3

Heat Flow Analysis

3.1 Introduction

Heat can be transferred by conduction, convection, and radiation in sediments (Beardsmore and Cull, 2001). The sediment–water–interface temperature and the basal heat flow are the main boundary conditions for heat flow analysis in sediments. Magnitude, orientation and distribution of the heat inflow at the base of the sediments are determined by mechanical and thermal processes of the crust and mantle (Allen and Allen, 2005). Two processes result in permanent heat flow from the Earth's interior to its surface: earth cooling and radiogenic heat production with a ratio of 17% to 83% respectively (Turcotte, 1980).

Heat conduction is defined as the transfer of thermal energy by contact according to thermal gradients. It is the primary process in the shallow lithosphere. The controlling lithological parameter is the thermal conductivity. It usually decreases from solids to liquids to gases. Generally, heat conduction is more effective with higher density.

Heat convection is thermal energy transported with the movement of a fluid or solid. In sedimentary basins, it is mainly related to fluid flow of pore water, liquid petroleum and gas. Convection can be more efficient than conduction when flow rates are high, e.g. in permeable layers or in fractures. It is the dominant thermal transport mechanism in the asthenosphere. Fluid movements can either add or remove thermal energy from a sedimentary sequence and can considerably distort conductive heat transfer systems. Solid convection occurs for example during overthrusting and salt doming. It requires very high thrusting rates to be of significance. A special type of combined conduction and convection is advection, which describes, for example, the heating of grains by groundwater flow.

Heat radiation is thermal transport via electromagnetic waves usually with wavelengths of 800 nm to 1 mm. The amount of thermal energy is proportional to the fourth power of temperature. Therefore, only heat transfer from very

T. Hantschel, A.I. Kauerauf, *Fundamentals of Basin and Petroleum Systems Modeling*, DOI 10.1007/978-3-540-72318-9_3,

hot areas requires attention. It is negligible in sediments, but should be considered in deep parts of the lithosphere or asthenosphere.

The heat conductivity law states, that a temperature difference between two locations causes a heat flow $\mathbf{q}$. Its magnitude depends on the thermal conductivity of the material and the distance between these locations. In mathematical notation it becomes

$$\mathbf{q} = -\boldsymbol{\lambda} \cdot \boldsymbol{\nabla} T \tag{3.1}$$

with the temperature gradient $\boldsymbol{\nabla} T$ and the thermal conductivity tensor $\boldsymbol{\lambda}$.

The tensor $\boldsymbol{\lambda}$ is often assumed to have only two independent components: the conductivity along a geological layer λ_h and the conductivity across a geological layer λ_v. The heat flow vector at any location is mainly directed along the steepest decrease of temperature from a given location. In the lithosphere, it is mainly caused by the difference between its top and base temperatures: the surface temperature or sediment–water–interface (SWI) temperature at the top and the asthenosphere–lithosphere boundary temperature at its base. Hence, the resulting heat flow is mainly vertically directed when the two boundary surfaces are almost spherical and when the lateral variations of the boundary temperatures are small. The average thermal conductivity and the thickness of the mantle and crustal layer mainly control the heat in–flux into the sediments. This heat flow at the base of the sediments defines the lower boundary condition for the heat flow analysis in the sediments.

In practice, heat flow analysis is commonly subdivided into two problems: the consideration of the crustal model to calculate the heat in–flux into the sediments and the temperature calculation in the sediments afterwards (Fig. 3.1).

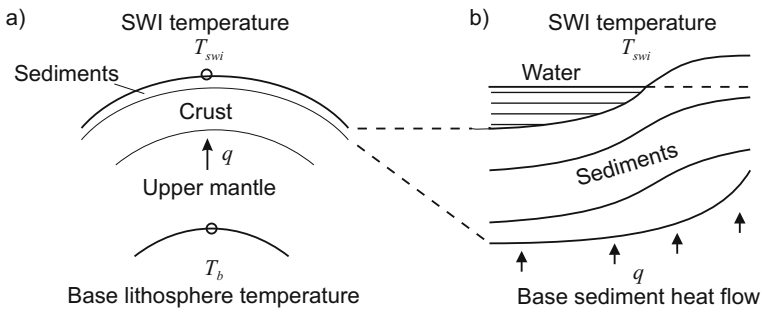

Fig. 3.1. Boundary value problem for a heat flow analysis (a) of the lithosphere and (b) in the sediments

3.2 One Dimensional (1D) Models

In the 1D approach, it is assumed that all heat flow vectors are directed vertically. 1D solutions often provide a good estimate for temperatures since the boundary values define radial core to surface aligned paths. They are especially used for well–based calibrations of basal heat flow trends. Exceptions, which cannot be modeled with 1D approaches are local areas of extraordinarily high thermal conductivities like salt domes, which bundle heat flow vectors from adjacent areas along highly conductive avenues.

3.2.1 Steady State Models

The most simple 1D models are steady state solutions in which all time dependent terms such as transient or convection effects are neglected. In the absence of radioactivity, the heat flow q is constant throughout the sediments and the temperature gradient in a layer is higher the lower the thermal conductivity. Multilayer solutions can then be directly derived from the heat flow equation (3.1) with the assumption that the average bulk thermal conductivity λ_b of a layer sequence is equal to the harmonic average of the corresponding single layer bulk thermal conductivities λ_i. The temperature controlled boundary value problem of the lithosphere yields the following 1D steady state solution with vertical thermal conductivity λ_b and thickness h_l of the lithosphere, and the corresponding properties of the upper mantle λ_m, h_m, the crust λ_c, h_c and sediments λ_s, h_s.

$$q = \lambda_b \frac{T_b - T_{\mathrm{swi}}}{h_l}, \quad \frac{h_l}{\lambda_b} = \frac{h_m}{\lambda_m} + \frac{h_c}{\lambda_c} + \frac{h_s}{\lambda_s} \,. \tag{3.2}$$

The advanced solution of the lithosphere problem, taking into account radioactive heat production, transient effects and convection caused by stretching, is discussed in Sec. 3.8. An equivalent steady state solution for the n–layer model of sediments with a base sediment heat flow q_{bs} can be derived from equation (3.1) for the temperature at base of the sediments T_{bs} and a temperature increase ΔT_i within a layer i as follows.

$$T_{bs} = T_{\mathrm{swi}} + \sum_{i=1}^{n} \Delta T_i, \quad \Delta T_i = q_{bs} \frac{h_i}{\lambda_i} \,. \tag{3.3}$$

The temperatures at all layer boundaries can be calculated from the surface temperature down to the base of section. This algorithm is illustrated in Fig. 3.2 for a simple sediment column consisting of only three lithotypes: shale, sandstone and limestone. The bulk conductivity for each layer λ_i is here approximated by a geometric average of the values for water λ_w and rock λ_r with the porosity ϕ as follows.

$$\lambda_i = {\lambda_r}^{(1-\phi)} {\lambda_w}^{\phi} \,. \tag{3.4}$$

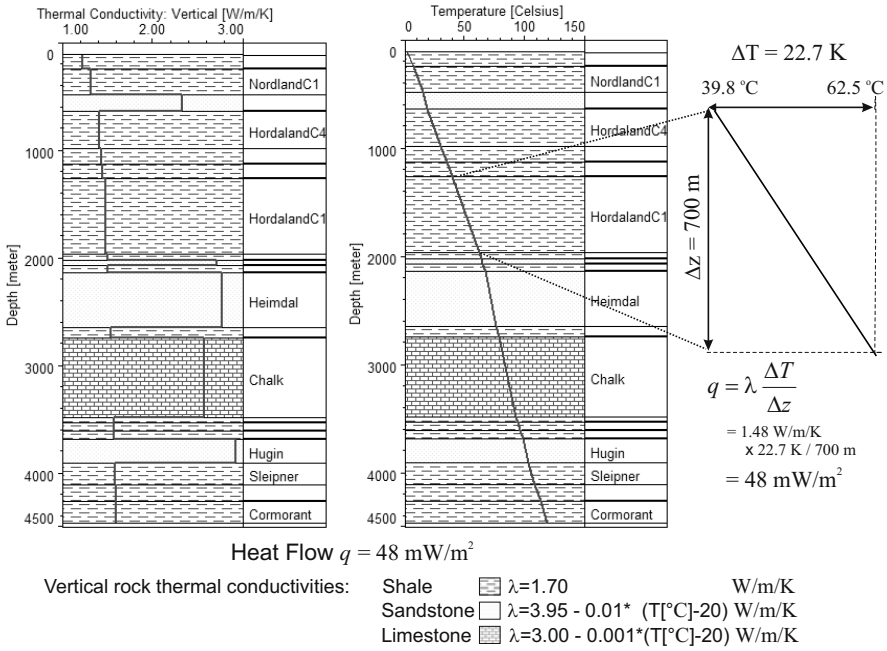

Fig. 3.2. 1D steady state example of a simplified model of a North Sea well. The bulk conductivity of the Hordaland Shale (1.48 W/m/K) is geometrically averaged from rock with $\lambda_r = 1.70$ W/m/K and water with $\lambda_w = 0.7$ W/m/K at a porosity of 15.6 %

The temperature–versus–depth curve clearly shows intervals of steep and low increases due to low and high values of bulk thermal conductivities. This simple steady state argumentation shows that a heat flow analysis which based on a constant thermal gradient is a very rough approximation.

However, the heat flow from the base upward does not remain constant because sediments contain radioactive elements like uranium, thorium and potassium. Radioactivity causes additional heat production, which increases the heat flow through the sediments. Thus, the surface heat flow is higher than the basal value by the amount of generated heat. Each of the radioactive elements generates gamma rays with radiogenic heat production rates Q_r estimated by Rybach (1973) as follows:

$$Q_r = 0.01\,\rho_r\,(9.52\,\mathrm{U} + 2.56\,\mathrm{Th} + 3.48\,\mathrm{K}) \tag{3.5}$$

where ρ_r is the rock density in kg/m^3, U and Th are the concentration of uranium and thorium in ppm, K is the concentration of potassium in % and Q_r is in μW/m^3. Pore fluids do not contribute to radioactive heat production. The resulting increase of vertical heat flow Δq in a layer of thickness h due to a rock heat production rate Q_r is as follows:

$$\Delta q = (1 - \phi)\, h\, Q_r \ . \tag{3.6}$$

The simple layer sequence example of Fig. 3.3 shows an average increase of the heat flow of about $1\,\mathrm{mW/m^2}$ per km sediment, which is a good general estimate.

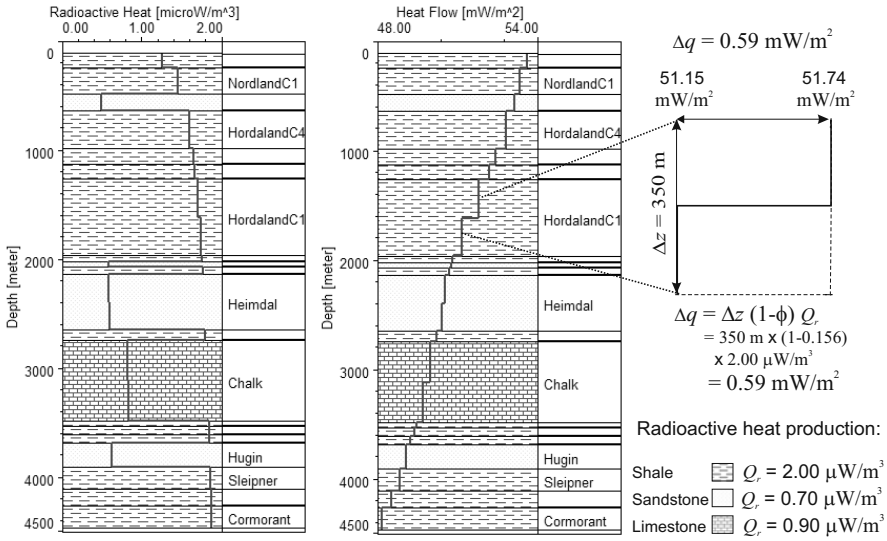

Fig. 3.3. Heat flow increase for the North Sea well with an example calculation in the Hordaland layer. The total increase of $5\,\mathrm{mW/m^2}$ from base to top is about $1\,\mathrm{mW/m^2}$ per km sediment

3.2.2 Transient Effect

A system is in thermal steady state when the heat flow is constant everywhere. Any change of a thermal boundary condition, geometry, properties or temperatures yields non-steady or transient state. The system will gradually return to a new flow equilibrium, when the new conditions do not change any more. The transition time depends generally on the ratio of the transported heat and the inner thermal energy, which is controlled by the size of the system, and ratio of the heat capacity and the thermal conductivity.

The transient 1D temperature distribution along the downward directed z–axis is the solution of the following differential equation:

$$\rho c \frac{\partial T}{\partial t} - \frac{\partial}{\partial z}\left(\lambda \frac{\partial T}{\partial z}\right) = Q_r \tag{3.7}$$

where c and ρ are bulk values, which should be arithmetically mixed from the pore fluid and rock values corresponding to the actual porosity. The transient effect is important during deposition and erosion and when thermal boundary conditions, namely SWI temperatures or basal heat flow, change rapidly.

Deposition results in deeper burial and higher temperatures of underlaying sediments. The actual sediment temperatures are lower than for the steady state solution. Heat is absorbed for heating of the layer and heat flow values decrease towards the surface. In case of constant deposition without compaction the heat flow decreases linearly in vertical direction (Fig. 3.4.a and b). It can indeed be analytically proven, that a constant deposition rate S yields a constant heat flow gradient after a relatively short time of deposition, according to (F.24) with

$$\frac{\partial q}{\partial z} \approx \frac{qS\rho c}{\lambda} \ . \tag{3.8}$$

The example values used in Fig. 3.4 result in a gradient of

$$\frac{\partial q}{\partial z}[\mathrm{mW/m^2/km}] = 3.678\, S[\mathrm{km/My}] \ . \tag{3.9}$$

In the case of erosion the effect is reverse: the sediment temperatures are higher than the steady state solution and the heat flow increases toward the surface. The above rule (3.8) can also be applied to estimate the magnitude of erosion–induced heat change (Fig. 3.4.c). During a hiatus the heat flow gradually returns to the steady state solution, with a constant heat flow value in regions without radioactivity.

The transient effect of an instantaneous heat flow change is shown in Fig. 3.5. Herein, the basal heat flow jumps from $40\,\mathrm{mW/m^2}$ to $60\,\mathrm{mW/m^2}$ while the near surface heat flow change is delayed for more than 5 Ma. Similar examples can be calculated analytically (App. F).

A change in SWI temperature also yields transient heat flow curves (Fig. 3.6). Typical SWI temperature variations yield much lower magnitudes compared to those caused by basal heat flow changes. Here, SWI or surface temperatures are average values over a range of 1000 to 10000 years. Seasonal cycles or short time changes are not taken into account. Sudden surface temperature rises lower the temperature difference between top and base and yield lower surface heat flow values. This effect occurs in glacial intervals of the quaternary period as shown in Fig. 3.21. The presented model uses small time steps of 2000 years for the approximation of the surface temperature variation. The temperature increases are especially steep and cause downward trends in the surface heat flow. Generally, near surface heat flow is correlated with the average surface temperatures of the previous thousands of years.

The heat flow is constant from base to top for 1D solutions without radioactivity and transient effects. Erosion and radiogenic sediments increases the surface heat flow, while deposition lowers surface heat flow. A transient solution of the 1D example model in Fig. 3.2 and Fig. 3.3 is shown in Fig. 3.7.

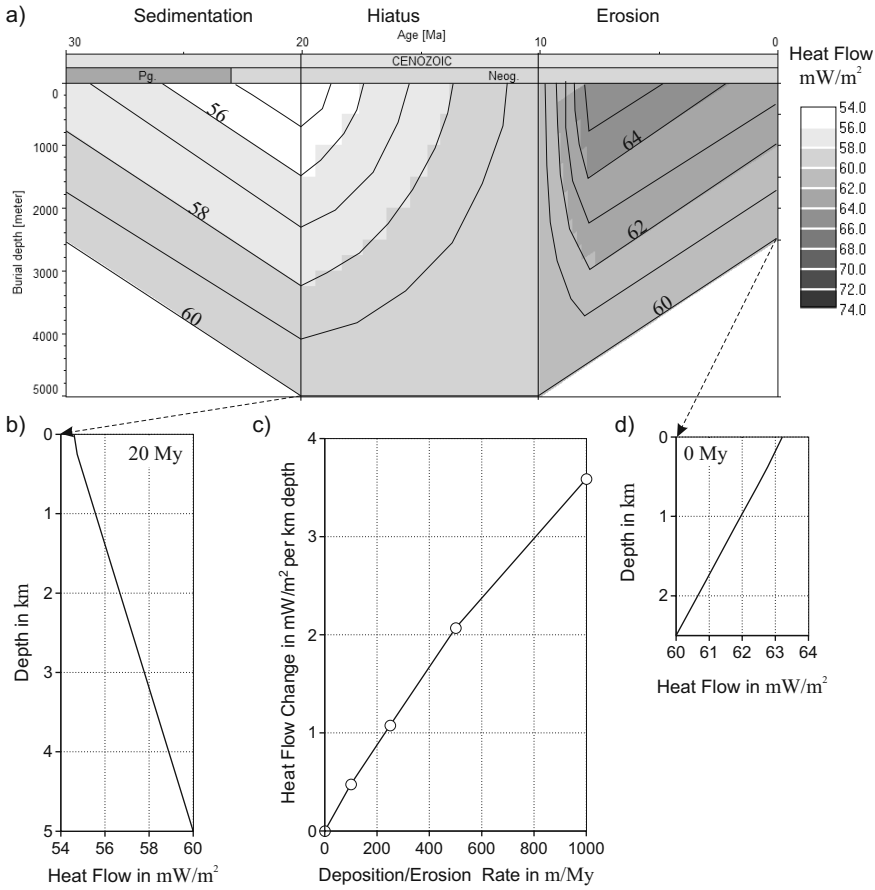

Fig. 3.4. Transient effect of deposition and erosion: (a) burial history with heat flow overlay for periods of uniform deposition, hiatus and uniform erosion. (b) Heat flow vs. depth after deposition. (c) Rate dependent heat flow change per 1000 m sediment. (d) Heat flow vs. depth after erosion. The example is calculated with a constant basal heat flow. Compaction is neglected

Herein, the basal heat flow variation through geological time is the main control on the heat flow in the well. However, the heat flow isolines are not perfectly vertical lines as radioactivity causes a significant slope. Figure 3.7.a shows calculated heat flow values for present day, without radioactivity, to quantify the transient effects. The transient effect of $0.8\,\mathrm{mW/m^2}$ is mainly controlled by deposition and it is much smaller than the increase of $6\,\mathrm{mW/m^2}$ caused by radioactivity.

It is often of interest to evaluate the difference between non–steady and steady–state thermal conditions in a basin. This can be done by solving the heat flow equation twice, once with and once without the transient term. The

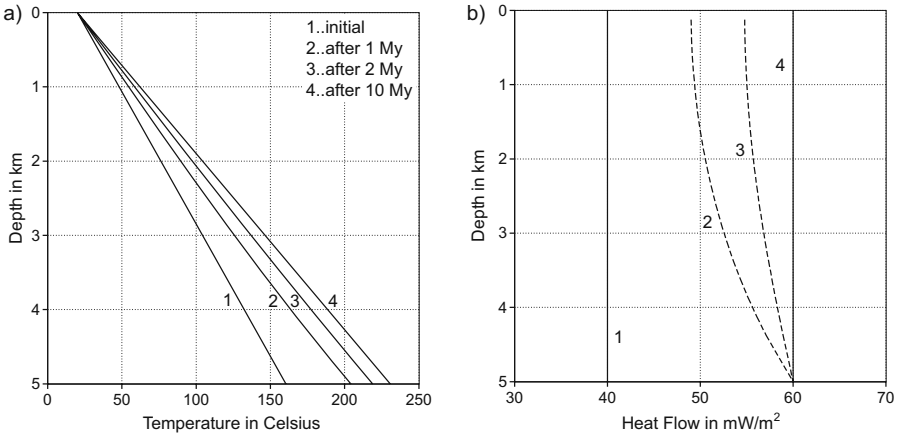

Fig. 3.5. Transient effect due to a basal heat flow switch

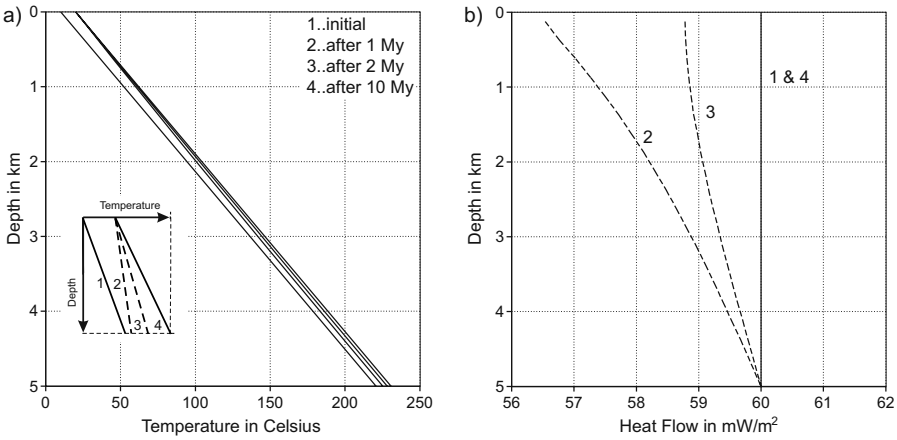

Fig. 3.6. Transient effect of SWI temperature change from 15°C to 25°C

difference between the two types of calculated temperature fields is called the "thermal disequilibrium indicator".

3.3 Thermal Conductivity

Thermal conductivity describes the ability of material to transport thermal energy via conduction. For a given temperature difference a good heat conductor induces a high heat flow, or a given heat flow maintains a small temperature difference. Steep temperature gradients occur in layers with low thermal conductivities. The unit for thermal conductivity is W/m/K.

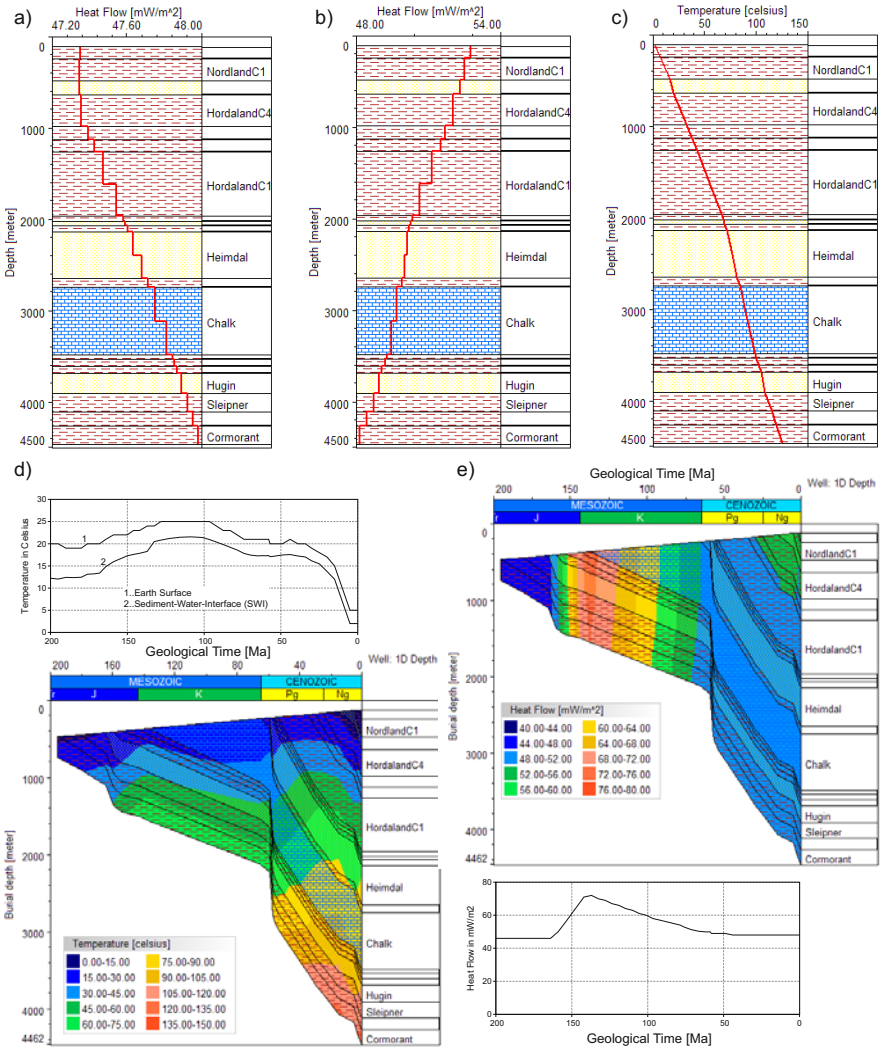

Fig. 3.7. 1D transient solution of a simplified model of a well in the North Sea. (a) Present day heat flow without radioactivity. (b),(c) Present day heat flow and temperature with radioactivity. (d) Temperatures during burial history and SWI temperature trend with radioactivity. (e) Heat flow values during burial history and basal heat flow trend with radioactivity

The bulk thermal conductivity is controlled by conductivity values of rock and fluid components. Mixing rules for rock and fluid components are generally complex and depend on whether the mixture is homogeneous or layered (Sec. 8.3). Sedimentary rocks are anisotropic with higher horizontal than vertical thermal conductivities. Generally, the thermal conductivity $\boldsymbol{\lambda}$ is a symmetrical tensor with six independent components. It is often considered to have only two independent components: the conductivity along the geological layer λ_h and the conductivity across the geological layer λ_v with an anisotropy factor $a_\lambda = \lambda_\mathrm{h}/\lambda_\mathrm{v}$.

3.3.1 Rock and Mineral Functions

Thermal conductivities commonly depend on temperature and vary widely according to the type of rock. Some 20°C values of vertical conductivities λ_v^{20} and anisotropy factors $a_\lambda^{20} = \lambda_\mathrm{h}^{20}/\lambda_\mathrm{v}^{20}$ are given in App. E.

Sekiguchi–Waples Model

The temperature dependence of matrix conductivity of any mineral, lithology, kerogen or coal can be calculated using the following equations adapted from Sekiguchi (1984) and plotted in Fig. 3.8.a.

$$\lambda_i(T) = 358 \times (1.0227\,\lambda_i^{20} - 1.882) \times \left(\frac{1}{T} - 0.00068\right) + 1.84 \qquad (3.10)$$

with $i = v, h$, λ in W/m/K and T in K.

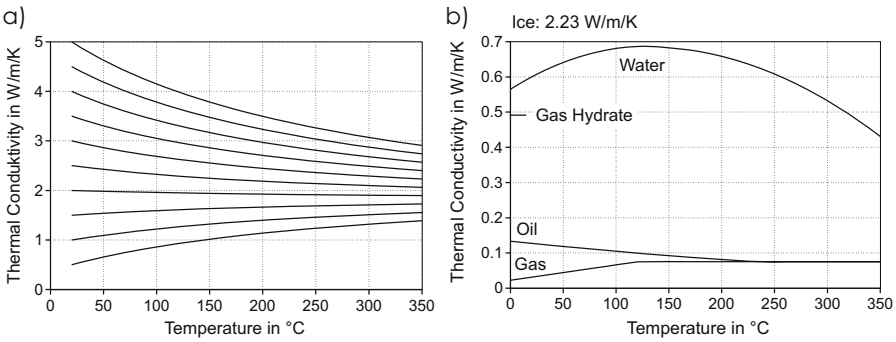

Fig. 3.8. Thermal conductivity functions: (a) rocks, (b) fluids

Most rocks and minerals do not experience significant changes in their anisotropy factors during compaction. Exceptions are claystones with significant dependency on compaction states. The effect can be described with a

factor f defining the ratio of the depositional vertical conductivity λ_{vd} to the vertical conductivity of rock with zero porosity λ_{v0}. The latter is an extrapolated value for a fully compacted rock. Horizontal conductivities are calculated using the principle of Waples and Tirsgaard (2002) assuming that the mean thermal conductivity value of the clay minerals $\lambda_m = \lambda_v + 2\,\lambda_h$ remains constant during compaction. It is further assumed that the decrease in vertical conductivity with compaction is exponential as follows:

$$\lambda_v(\phi) = \lambda_{v0} f^{\phi/\phi_0} \tag{3.11}$$

where λ_{v0} is the vertical conductivity of an ideally compacted rock with $\phi = 0$, ϕ_0 is the depositional porosity and f is the grain rotation factor with $f = 1$ for porosity independent anisotropy.[1] The principle of constant mean conductivity yields a porosity dependent horizontal conductivity $\lambda_h(\phi)$ from the horizontal conductivity of an ideally compacted rock λ_{h0} as follows:

$$\lambda_h(\phi) = \lambda_{h0} + \frac{1}{2}\left(\lambda_{v0} - \lambda_v(\phi)\right) . \tag{3.12}$$

Thus, the conductivity values of a rock with any porosity and temperature are calculated in two steps. First, the porosity related corrections are made using (3.12) for claystones only and second, the temperature corrections are made using (3.10) for both (vertical and horizontal) values separately.

In the following example, the matrix thermal conductivity values of a shale with $\lambda_{v0}^{20} = 1.64\,\mathrm{W/m/K}$, $a_\lambda = 1.6$, $\phi_0 = 70\%$ and $f = 1.38$ are calculated at $\phi = 30\%$ and $T = 80°\mathrm{C}$:

$$\begin{aligned}
\lambda_{h0}^{20} &= 1.60 \times 1.64 = 2.624 \\
\lambda_{v\phi}^{20} &= 1.64 \times 1.38^{0.3/0.7} = 1.883 \\
\lambda_{h\phi}^{20} &= (1.64 + 2 \times 2.624 - 1.883)/2 = 2.520 \\
\lambda_v &= 358 \times (1.0227 \times 1.883 - 1.882) \times (0.00283 - 0.00068) + 1.84 = 1.876 \\
\lambda_h &= 358 \times (1.0227 \times 2.520 - 1.882) \times (0.00283 - 0.00068) + 1.84 = 2.402
\end{aligned}$$

The complete thermal conductivity versus porosity functions of the above example shale are shown in Fig. 3.9.

Linear Dependency Model

A simplified alternative model for rock matrix conductivities is based on the assumption of linearly temperature dependent values only.

[1] Anisotropy values are often given by the depositional conductivity λ_{vd}, the fully compacted conductivity λ_{v0} at $\phi = 0$ and anisotropy factors $a_{\lambda d} = \lambda_{hd}/\lambda_{vd}$, $a_{\lambda 0} = \lambda_{h0}/\lambda_{v0}$. The constant sum of horizontal and vertical conductivities becomes $\lambda_{vd}(1 + 2a_{\lambda d}) = \lambda_{v0}(1 + 2a_{\lambda 0})$ and therefore $f = (2a_{\lambda 0} + 1)/(2a_{\lambda d} + 1)$.

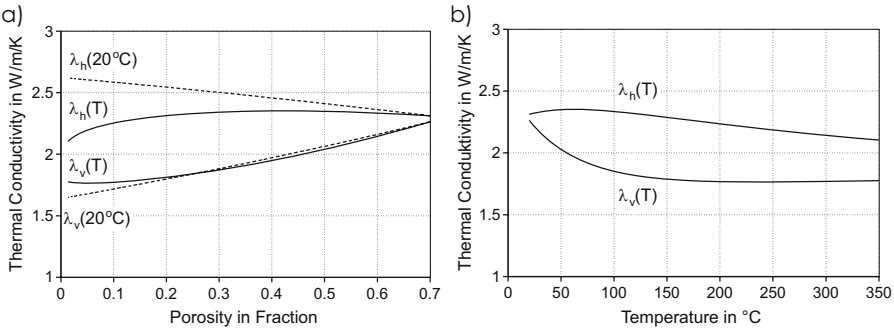

Fig. 3.9. Rock thermal conductivity functions of a typical shale under hydrostatic compaction and a constant temperature gradient of 30°C/1000 m with a temperature $T = 20\,°C$ at deposition. (a) Porosity dependency (b) Temperature dependency

$$\lambda_v(T) = \lambda_v^{20} + \lambda_T\,(T - 20°\mathrm{C}) \tag{3.13}$$

where λ_v^{20} is the thermal conductivity at 20°C and λ_T is the conductivity increase per degree temperature. Default values for some lithologies are listed in App. E. Such a linear temperature dependency is often assumed in an interval from −20°C to 300°C.

Rock Mixtures

Mineral component based matrix conductivity values are calculated with the geometric average of their component minerals when the minerals are homogeneously distributed in the rock (Fig. 8.4). The geometrical average is also used for rocks consisting of homogeneously distributed lithological components. In the case of layered structures the horizontal conductivities are calculated with arithmetic averages and the vertical conductivities with harmonic averages.

3.3.2 Pore Fluid Functions

Thermal conductivities of fluids are isotropic and depend on temperature (Fig. 3.8). Deming and Chapman (1989) published the following formulas for water:

$$\lambda_w = \begin{cases} 0.565 - 1.88 \times 10^{-3}\,T - 7.23 \times 10^{-6}\,T^2 & \text{for} \quad T < 137°\mathrm{C} \\ 0.602 - 1.31 \times 10^{-3}\,T - 5.14 \times 10^{-6}\,T^2 & \text{for} \quad T > 137°\mathrm{C} \end{cases} \tag{3.14}$$

with λ_w in W/m/K and T in Kelvin.

The following equations for conductivities of liquid and vapor petroleum are based on Luo et al. (1994) and a personal communication between Ming Luo and Doug Waples.

$$\begin{aligned}
\lambda_o &= 0.2389 - 4.593 \times 10^{-4}\, T + 2.676 \times 10^{-7}\, T^2 && \text{for} \quad T < 240°\text{C} \\
\lambda_g &= -0.0969 + 4.37 \times 10^{-4}\, T && \text{for} \quad T < 120°\text{C} \\
\lambda_o &= \lambda_g = 0.075 && \text{else}
\end{aligned} \tag{3.15}$$

with λ_o and λ_g in W/m/K and T in Kelvin. Most hydrocarbon components approach conductivities of about 0.075 W/m/K at high temperatures (Poling et al., 2001). Similarly, methane conductivities also approach values close to 0.075 W/m/K (Lide, 2006). These results seem intuitively reasonable, since under those conditions both phases are supercritical and similarities of the properties dominate.

The thermal conductivity of solid pore substances, such as gas hydrates (clathrates) and ice, are 0.49 W/m/K, and 2.23 W/m/K, respectively (Sloan, 1998). All the above thermal conductivities are shown together in Fig. 3.8.b. Water is a superior thermal conductor, while gas has the lowest conductivity which yields isotherm bending below gas accumulations (Fig. 3.10).

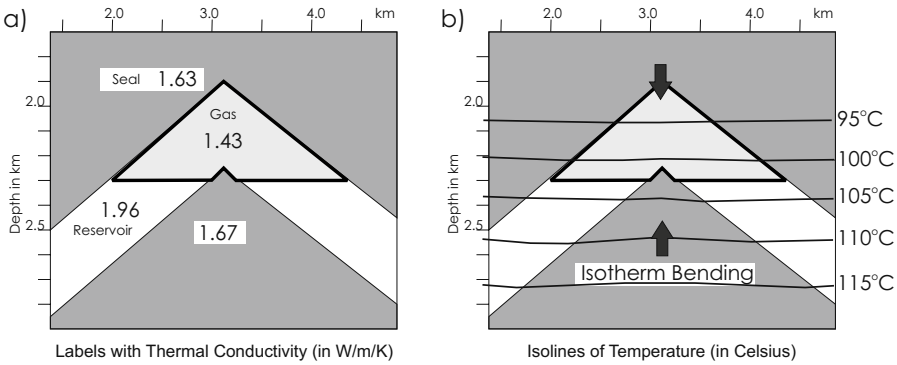

Fig. 3.10. Thermal effects of gas accumulations: (a) vertical bulk thermal conductivities, (b) isotherm bending

If the pore filling is a mixture of several (fluid or solid) phases then the geometrical average of the phase values is used. For water, liquid petroleum and gas it is

$$\lambda_p = (\lambda_w)^{S_w} (\lambda_o)^{S_o} (\lambda_g)^{S_g} \tag{3.16}$$

where λ_p is the pore fluid thermal conductivity, λ_w, λ_o, λ_g are the thermal conductivities of water, oil, and gas phases and S_w, S_o, S_g are water, oil, and gas saturations. The bulk thermal conductivity is obtained by averaging the rock matrix and pore values with the geometrical average

$$\lambda = \lambda_r{}^{(1-\phi)}\, \lambda_p{}^{\phi}\,. \tag{3.17}$$

A better but more complicated mixing rule is proposed by Buntebarth and Schopper (1998) based on mixing rules for spherical voids in a matrix.

$$\lambda = \lambda_r \frac{1 - E\phi}{1 + \alpha E\phi} \quad \text{with} \quad E = \frac{1 - Z}{1 + \alpha Z} \quad \text{and} \quad Z = \frac{\lambda_p}{\lambda_r} \,. \tag{3.18}$$

The authors propose a value of $\alpha = 5$ for water. This yields the following simplified law:

$$\lambda = \frac{\lambda_r + 5\lambda_p + \phi(\lambda_p - \lambda_r)}{\lambda_r + 5\lambda_p + 5\phi(\lambda_p - \lambda_r)} \,. \tag{3.19}$$

The whole procedure of calculating bulk conductivity values is summarized in Fig. 3.11.

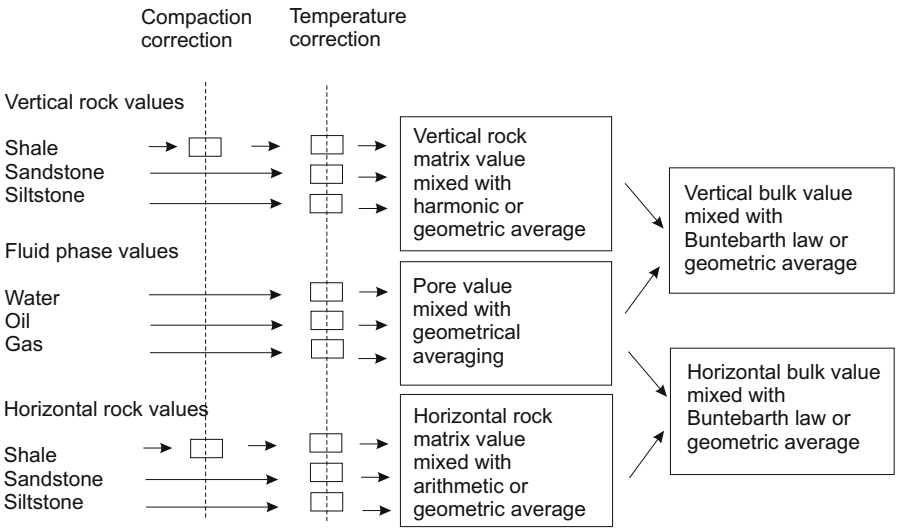

Fig. 3.11. Mixing of bulk thermal conductivities. The compaction and temperature corrections are described, e.g. with equations (3.11), (3.12), and (3.10)

3.4 Specific Heat Capacity

The heat capacity at constant pressure C_p is the ratio of a small (infinitesimal) amount of heat ΔQ absorbed from a body which increases the temperature by ΔT

$$C_p = \left(\frac{\Delta Q}{\Delta T}\right)_p \,. \tag{3.20}$$

The specific heat capacity or specific heat is defined as heat capacity per mass $c = C_p/m$.

The unit of specific heat is J/kg/K. The specific heat of a rock sample is measured by determining the temperature changes and the corresponding amount of heat entering or leaving the sample. The specific heat capacity is therefore the storage capacity for heat energy per unit mass. The ratio of the heat capacity and the thermal conductivity is a measure of the transient effect.

Heat capacity also controls the magnitude of convection as it determines how much of the stored heat can be moved together with a moving body. The specific heat capacity is a volumetric type property (Sec. 8.3). Rock and fluid component values are mixed arithmetically.

3.4.1 Rock and Mineral Functions

Specific heat capacities depend on temperature. The 20°C values c_{20} for minerals and some standard lithotypes are tabulated in App. E.

Waples Model

The temperature dependency of the heat capacity for any mineral, lithology, or rock value except kerogen and coal can be calculated using the following equation, which has been adopted from Waples and Waples (2004a) and is shown in Fig. 3.12.a.

$$c(T) = c_{20}\,(0.953 + 2.29 \times 10^{-3}\,T - 2.835 \times 10^{-6}\,T^2 + 1.191 \times 10^{-9}\,T^3) \quad (3.21)$$

where c_{20} is the heat capacity at 20°C and the temperature is given in °C. Waples and Waples (2004a) also proposed a special function for heat capacity of kerogen and coal as follows:

$$\begin{aligned} c(T)[\mathrm{J/kg/m}] = {} & 1214.3 + 6.2657\,T - 0.12345\,T^2 + 1.7165 \times 10^{-3}\,T^3 \\ & - 1.1491 \times 10^{-5}\,T^4 + 3.5686 \times 10^{-8}\,T^5 - 4.1208 \times 10^{-11}\,T^6\,. \end{aligned} \quad (3.22)$$

Linear Dependency Model

The temperature dependency can be approximated with a simple linear function.

$$c(T) = c_{20} + c_T\,(T - 20°\mathrm{C}) \quad (3.23)$$

where c_{20} is the heat capacity at 20°C, c_T is the heat capacity increase per degree temperature. Default lithological values for c_{20} and c_T are tabulated in App. E for a temperature interval from −20°C to 300°C.

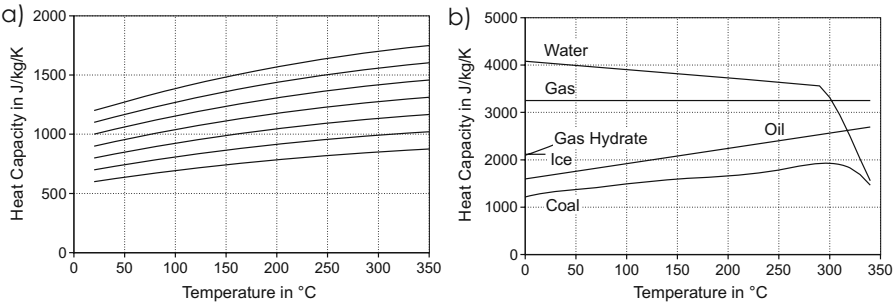

Fig. 3.12. Heat capacity for: (a) rocks, (b) coal and fluids

3.4.2 Pore Fluid Functions

Somerton (1992) developed equations for the specific heat capacity of pure water c_w as a function of temperature. For a relatively constant density the heat capacity decreases linearly to 290°C followed by a strong decrease at higher temperatures according to

$$\rho\, c_w = \begin{cases} 4245 - 1.841\, T & \text{for} \quad T < 290°\text{C} \\ 3703\, \exp[-0.00481\,(T-290)+ & \\ \quad 2.34 \times 10^{-4}\,(T-290)^2] & \text{for} \quad T < 290°\text{C} \end{cases} \tag{3.24}$$

with c_w in J/m/K, ρ in kg/m^3 and T in °C. The above described temperature dependent function is shown in Fig. 3.12.b assuming a constant water density of 1040 kg/m^3. According to Kobranova (1989) the specific heat of saline water is slightly lower than that of pure water.

Gambill (1957) published the equation below for the specific heat capacity of oil c_o as a function of temperature and density:

$$c_o = (1684 + 3.389\, T)\sqrt{\rho} \tag{3.25}$$

with c_o in J/m/K, ρ in kg/m^3, and T in °C. It is satisfactory to use a value for the specific heat capacity of natural gas for all compositions at all temperatures and pressures. A reasonable value is 3250 J/kg/K (Waples and Waples, 2004b). Waples also proposed the following equation for the heat capacity of gas hydrates $c_h$in the same paper.

$$c_h = 2097 + 7.235\, T + 0.0199\, T^2 \tag{3.26}$$

with c_h in J/m/K and T in °C. The specific heat capacity of ice (2115 J/kg/K) is about half that of liquid water for temperatures around 0 °C. The pore and bulk values of heat capacity values are mixed arithmetically.

3.5 Radiogenic Heat

Some minerals and rocks contain traces of the radioactive elements uranium (U), thorium (Th) and potassium (K) which are additional heat sources (3.5). Measurements and data catalogs are sparse, but D. Waples developed a data base for most rocks and minerals based on modeling experience and some literature data (App. E). These values should be used carefully especially since the effects on heat flow calculations are tremendous as was discussed in Sec. 3.2.1. Radiogenic heat values for lithologies are given as rock matrix values and are converted to bulk values during simulation by multiplying by $(1-\phi)$. They can be derived from the following data sources:

- uranium, thorium and potassium concentrations from spectral gamma ray measurements. These values are bulk values with a core sample porosity ϕ_c. One has to use Rybachs law (3.5) and divide by $(1-\phi_c)$ to get the corresponding matrix heat flow production rate Q_r.
- Gamma Ray API values. Buecker and Rybach (1996) proposed the following law to convert Gamma Ray APIs to matrix heat flow production values:

$$Q_r[\mu\mathrm{W/m^3}] = 0.0158\,(\mathrm{API} - 0.8)\ . \tag{3.27}$$

Concentrations of radioactive elements are present-day values U_0, T_0, K_0. Paleo-values are higher corresponding to their half-lives as follows (with t in My).

$$\begin{aligned} \mathrm{U} &= \mathrm{U}_0\,(1 + 2.77\times10^{-4}\,t - 7.82\times10^{-8}\,t^2 + 4.53\times10^{-12}\,t^3) \\ \mathrm{Th} &= \mathrm{Th}_0\,\exp(0.00005\,t) \\ \mathrm{K} &= \mathrm{K}_0\,\exp(0.000555\,t)\ . \end{aligned} \tag{3.28}$$

Uranium consists of two isotopes having different half–lives. The sum of the two exponential functions is approximated by a third order polynomial. The time correction is small on geological time scales.

3.6 Three Dimensional Heat Flow Equation

In 1D models, heat flows vertically upward from base to top. In multi–dimensional problems, heat flow can also laterally divert to follow layers of high thermal conductivity. The formulation of the multi-dimensional heat flow problem yields a transport–type differential equation with temperature as the field variable and heat flow as the corresponding flow variable. The heat transport equation is based on energy balances, which means that the temperature induced internal energy change in a volume element is equal to the heat conducted into or out of the volume element plus the heat transferred by convection plus radiogenic heat production. It is

$$\rho c \frac{\partial T}{\partial t} - \boldsymbol{\nabla} \cdot \boldsymbol{\lambda} \cdot \boldsymbol{\nabla} T = \rho_p c_p \boldsymbol{\nabla} \cdot (\mathbf{v}_p T) + Q_r \tag{3.29}$$

where $\boldsymbol{\lambda}$, ρ, c are the bulk thermal conductivity tensor, bulk density, and bulk specific heat capacity, v_p, ρ_p, c_p are the pore fluid velocity vectors, density, and specific heat capacity and Q_r is the bulk radioactive heat production.

The full heat flow problem with boundary conditions is shown in Fig. 3.13. The four main terms in the heat flow equation describe the transient effect, heat conduction, heat convection, and the influence of heat sources, respectively. Two material parameters control the magnitude of the effects: thermal conductivity for heat conduction and heat capacity for transient effects and convection. The same temperatures for rock and pore fluid are assumed. For fast moving pore fluids, different temperatures have to be considered instead.

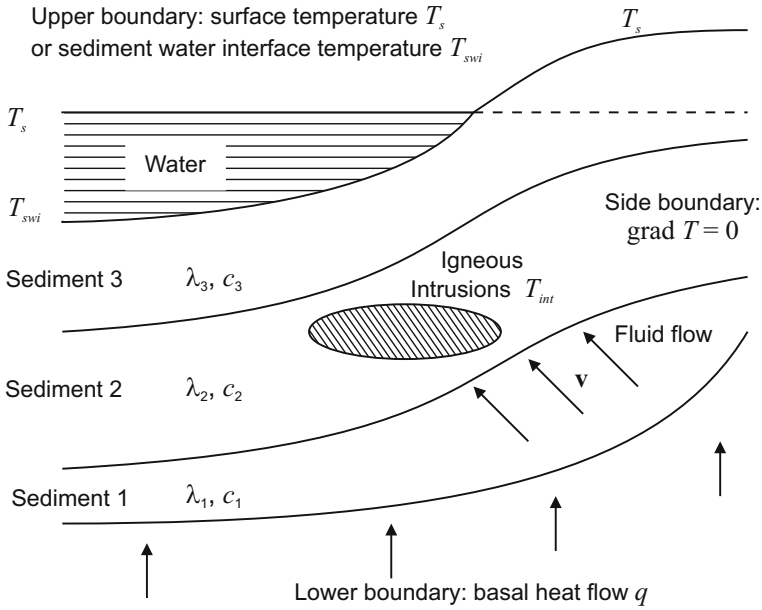

Fig. 3.13. Boundary value problem for the heat flow analysis

Temperatures or heat flow values have to be defined at all model boundaries. Common thermal boundary conditions are surface temperature (onshore) or sediment–water–interface (SWI) temperature (offshore) at the top of the sediments $T = T_{\mathrm{swi}}$, basal heat flow at the sediment base $q = q_b$ and no heat flow $\mathbf{n} \cdot \boldsymbol{\nabla} T = 0$ at the basin sides (Fig. 3.14.a). All boundary conditions have to be defined through geological time as paleo SWI temperatures and paleo heat flow trends, respectively. The lower boundary condition can alternatively be defined partially or completely with fixed base temperatures (Fig. 3.14.b and c). A deep isotherm map for the definition of the lower ther-

mal boundary can also be applied. Then, the model is subdivided into two domains and each of them is separately solved (Fig. 3.14.d).

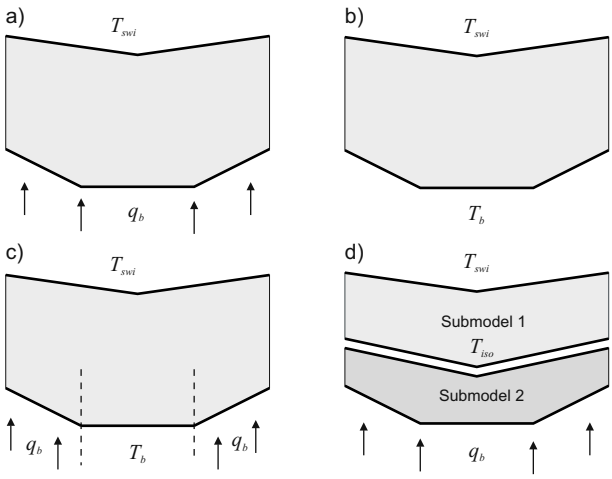

Fig. 3.14. Various types of boundary conditions

Three dimensional effects are important when large variations of the thermal conductivities occur. Salt has much higher conductivities than most other sediments. Thus, salt domes bundle heat flow as shown in Fig. 3.15.a. The preservation of the total energy requires that the heat flow adjacent to the dome has a corresponding lower value. The surface heat flow reflects this effect as well. The corresponding isotherms (Fig. 3.15.b.) bend down at the base of the salt due to higher salt conductivities. They also form a bow upwards at the top of the salt dome due to the higher heat flow values which is a typical 3D-effect and cannot be found in multi–1D models.

Calculated temperature and heat flow distributions of a multi–dimensional model are shown in Figs. 3.16 and 3.17. Thermal conductivities of the clastic rocks increase with depth according to the lower content of pore water, while salt domes are zones of high thermal conductivities. Shales correlate with very high radioactive heat sources. Heat flow from base to top generally increases due to radioactive heat production and it is concentrated along the high conductive salt domes and causes the bending of the isotherms as previously discussed. The higher surface heat flow above the salt domes can be clearly observed in the 3D–model. In such complex situations multi–1D models fail and show errors of more than 50°C (Fig. 3.17).

Some multi–dimensional schematic models can be solved analytically and the results can be used for "benchmarking" of simulation programs. The solutions of the following problems are given and discussed in the Appendix: influence of radiogenic heat production on steady state temperature (App. F.1),

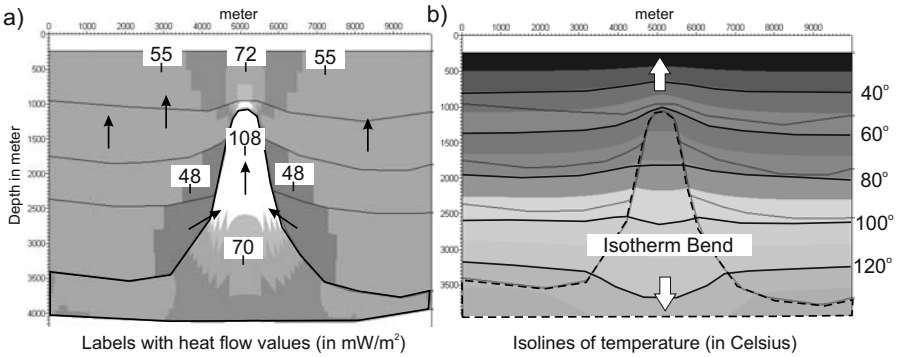

Fig. 3.15. Heat flow through a salt dome: the basal heat flow is $60\,\mathrm{mW/m^2}$ along the entire sediment base. The actual heat flow within the sediments increases to $108\,\mathrm{mW/m^2}$ within the dome. Note that heat flows near but outside the dome are lower than the basal heat flow

influence of lateral basal heat jump on temperature (App. F.2), influence of SWI temperature jump on temperature profiles (App. F.3), the steady state temperature field for a two block model (App. F.4), the transient temperature field of a model with basal heat flow jump (App. F.5), the transient temperature field of a model with SWI temperature jump (App. F.6).

3.6.1 Heat Convection

Heat convection is related to moving masses, solid and liquid. In sediments, heat convection is mainly caused by water flow. Water velocities are calculated when solving the pressure–compaction equations and so the convection term couples heat and fluid flow calculations. The amount of heat ΔQ transfered between two points with a temperature difference ΔT for a moving water mass m_w is

$$\Delta Q = c_w\, m_w\, \Delta T = c_w\, \rho_w\, V_w\, \Delta T \tag{3.30}$$

where c_w, ρ_w and V_w are the specific heat capacity, the density, and transported volume of the water. The corresponding convective heat flow $\mathbf{q}_v$ of water moving trough a cell with a length l, a slice–plane A, a bulk volume $V = A\,l$, and a velocity $\mathbf{v}_w$ is as follows:

$$q_v = \frac{\Delta Q}{A \Delta t} = \frac{c_w\, \rho_w\, \phi\, V\, \Delta T}{A \Delta t} = c_w\, \rho_w v_w\, \Delta T\ . \tag{3.31}$$

The above equation yields a convective heat flow value of $q_v = 0.04\,\mathrm{mW/m^2}$ with a water velocity of $1\,\mathrm{mm/y}$, a temperature difference of 1°C between the flow boundaries, a porosity $\phi = 0.3$, a heat capacity of $c_w = 4186\,\mathrm{J/kg/K}$, and a water density $\rho_w = 1035\,\mathrm{kg/m^3}$. Compaction and overpressure driven water velocities are much smaller. Hence compaction driven convection can

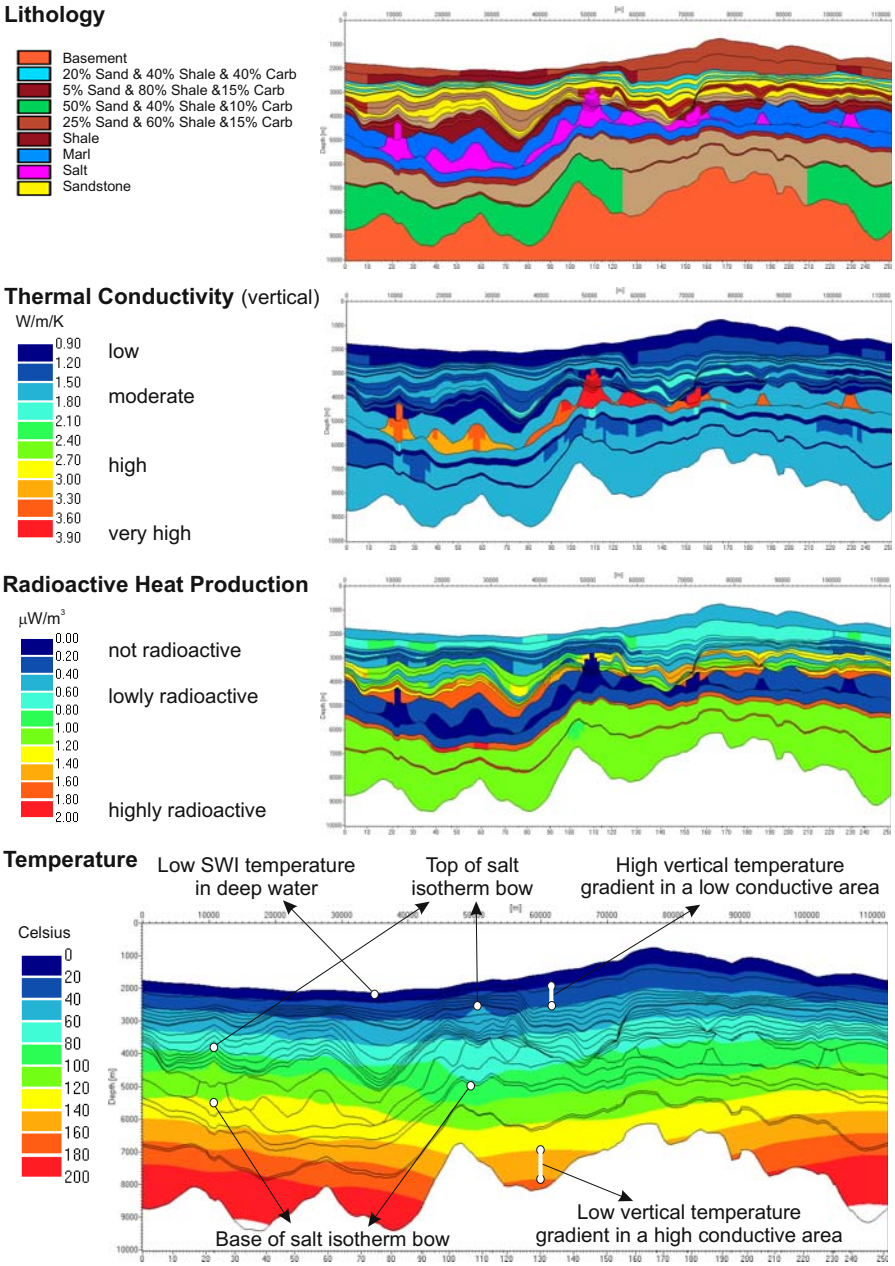

Fig. 3.16. Multi–dimensional heat flow analysis part I, cross-section from Campos Basin, Brazil. The present day temperature distribution shows several multi–dimensional effects like isotherm bending around salt, SWI temperature variation in deep water and temperature gradient variations according to the thermal conductivities

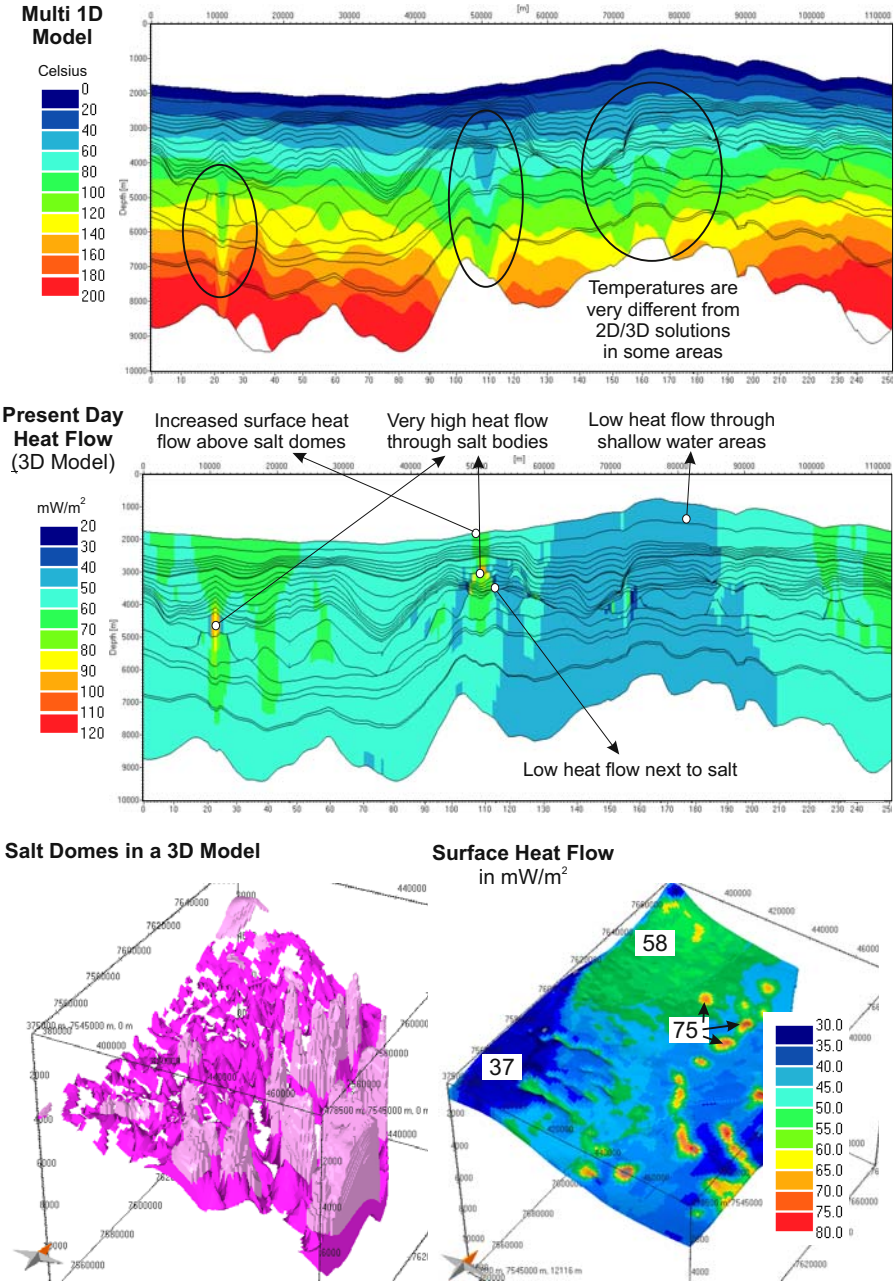

Fig. 3.17. Multi–dimensional heat flow analysis part II, multi–1D temperature model, multi–dimensional heat flow distribution at present day and surface heat flow anomalies above salt domes for a 3D model

be neglected in the thermal budget. Topographically driven aquifer flow and flow of hot water through high permeable fractures and faults can have higher flow velocities and must for that reason be taken into account.

3.6.2 Magmatic Intrusions

Magmatic intrusions can have substantial effects on paleo–temperatures and all thermal calibration parameters. Although the duration of such events is relatively short, extremely high temperatures can trigger rapid chemical reactions in the adjacent environment. Igneous intrusions are modeled with the magmatic temperature as inner boundary condition at the location and time of the intrusion. In subsequent time steps, the temperature decreases in both the intrusion and the surrounding layers. Then, hot liquid magma crystallizes to solid rock. The related crystallization heat is important and has to be taken into account in the heat balance. The principal processes together with some typical values according to Delaney (1988) are shown in Fig. 3.18. Here, it is necessary to switch the lithological properties of the intrusion volume elements twice, at the time of intrusion and again at the time of solidification.

The temperature development during cooling in a simple example is shown in Fig. 3.19, where effects on temperature can still be seen 100,000 years after the time of intrusion. Older intrusions can be recognized in vitrinite reflectance peaks in the vicinity of the intrusions. The use of smaller time steps after the time of intrusion is necessary. Time steps of 500 y, 1 000 y, 2 000 y, 5 000 y, 10 000 y, 20 000 y, 50 000 y, 100 000 y yield suitable results.

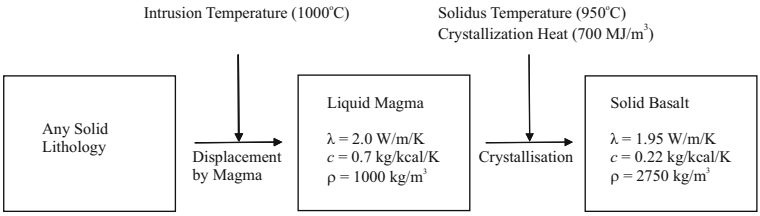

Fig. 3.18. Intrusion model and default values from Delaney (1988)

3.6.3 Permafrost

Modeling permafrost requires the introduction of permafrost lithologies with ice in the pores instead of water. Furthermore, additional heat sources and sinks for ice solidification and melting have to be taken into account. The trigger parameter for converting a lithology into a permafrost lithology is a temperature of 0.7 °C. Hence, temperatures below permafrost are much lower

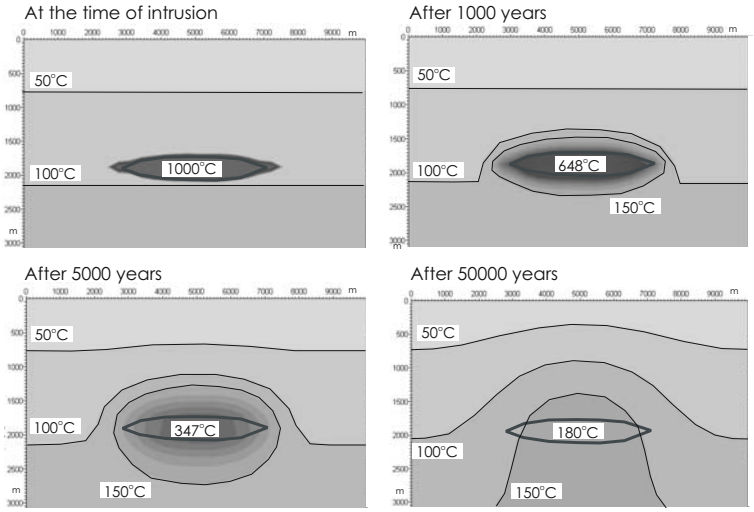

Fig. 3.19. Temperature development around an intrusion of size 300 m × 3000 m

compared to ice–free periods (Fig. 3.20). The high thermal conductivity of ice $\lambda = 2.33\,\mathrm{W/m/K}$ compared to liquid water yields low temperature gradients (Fig. 3.20) and supports the cooling effect. The cooling is further increased by the solidification heat of ice $Q_s = 335\,\mathrm{J/kg}$, which is removed from the permafrost environments. The specific heat capacity of ice (0.502 J/kg/m) is relatively small compared to water.

Modeling the sequence of interglacial periods such as in the Pleistocene, requires the use of very small time steps of about 1000 years to get an appropriate solution for the fluctuations in surface temperature and the corresponding surface heat flow (Fig. 3.21). The surface heat flow peaks generally coincide with the steep changes in surface temperatures, which especially occurred during the change from cold to warm periods.

Ice loading can also be simulated in permafrost periods. Then, an uppermost layer is introduced with the thermal and mechanical properties of pure ice. This yields special characteristics of pore- and lithostatic pressure curves as shown in Fig. 3.21.

3.7 SWI Temperatures

The sediment–water–interface temperature T_{swi} or bottom–water–temperature is the upper boundary for the heat flow problem. It can be determined with estimated paleo mean surface or air temperatures T_s and corrections for water depths. The annual mean ground surface temperature is primarily obtained from mean air temperatures (www.worldclimate.com), which depends

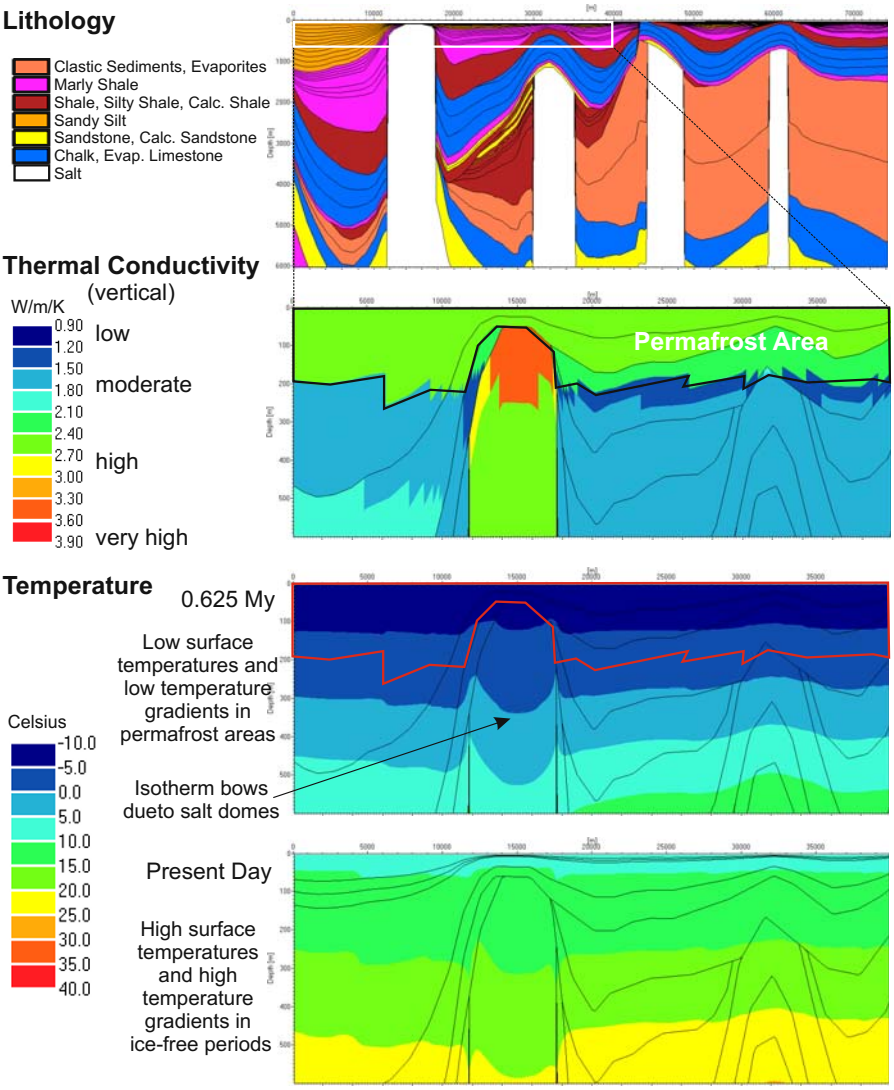

Fig. 3.20. Heat flow analysis in a permafrost area, sample cross–section from the Lower–Saxony Basin, Germany (Grassmann et al., 2005; Delisle et al., 2007). The model has a 200 m thick permafrost layer with very high conductivities at 0.625 My. The resulting temperature gradients differ significantly from the ice free present day temperatures. The thermal conductivities in the salt are generally very high

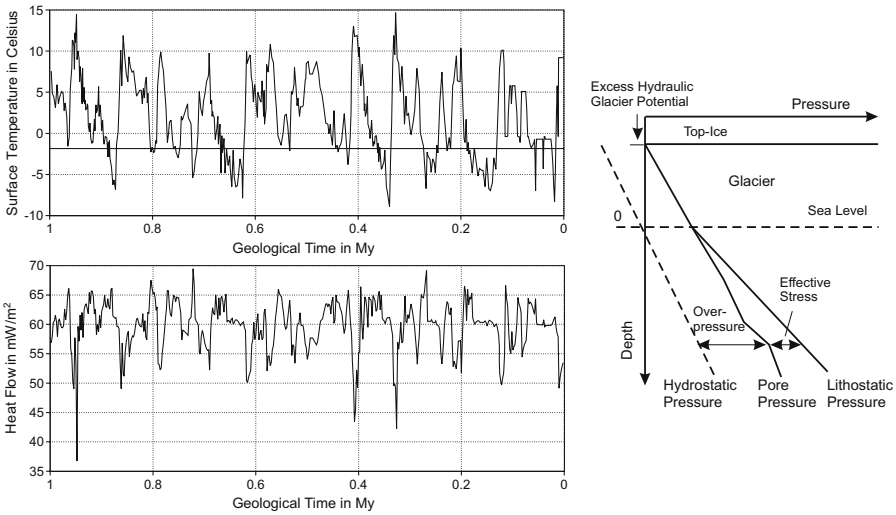

Fig. 3.21. Heat and pressure analysis in a Pleistocene sample cross–section of Fig. 3.20. The surface heat flow is low when the surface temperature increases and visa versa. The glacier causes an excess hydraulic potential on the top glacier surface

on latitude. Beardsmore and Cull (2001) proposed the following latitude and water depth dependent equation for the present day sediment–water–interface temperature with an error bar of 2 °C.

$$\begin{aligned} \ln(T_{\text{swi}} - T_f) &= a + b \ln z \,, \\ T_f &= -1.90 - 7.64 \times 10^{-4}\, z \,, \\ a &= 4.63 + 8.84 \times 10^{-4}\, L - 7.24 \times 10^{-4}\, L^2 \,, \\ b &= -0.32 + 1.04 \times 10^{-4}\, L - 7.08 \times 10^{-5}\, L^2 \end{aligned} \tag{3.32}$$

where T_f is the freezing temperature in °C, z is the water depth in m, and L is the latitude in degree. The corresponding SWI temperature versus depth curves are shown in Fig. 3.22.

An average air surface temperature history is given in Fig. 3.23 for different latitudes (Wygrala, 1989). Knowledge of the paleo latitude changes through geological time is therefore necessary to be able to derive paleo surface temperatures. This is shown in Fig. 3.24 for several continental areas.

The derivation of the paleo–SWI temperatures from average surface temperature is very difficult to estimate. Wygrala (1989) proposed a decrease of 1.5°C per 100 m in shallow water. The temperature in water deeper than 400 m is primarily controlled by the coldest arctic water temperatures T_n, which are presently affected by polar glaciations. A linear interpolation between the following three fixed points is a common approximation for a water depth based SWI temperature correction.

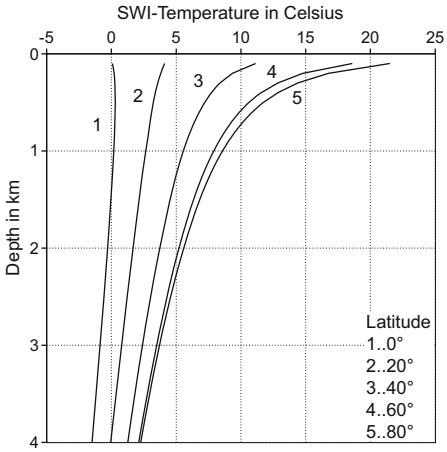

Fig. 3.22. Present day sediment–water–interface curves dependent on latitude and depth according to equation (3.32) after Beardsmore and Cull (2001)

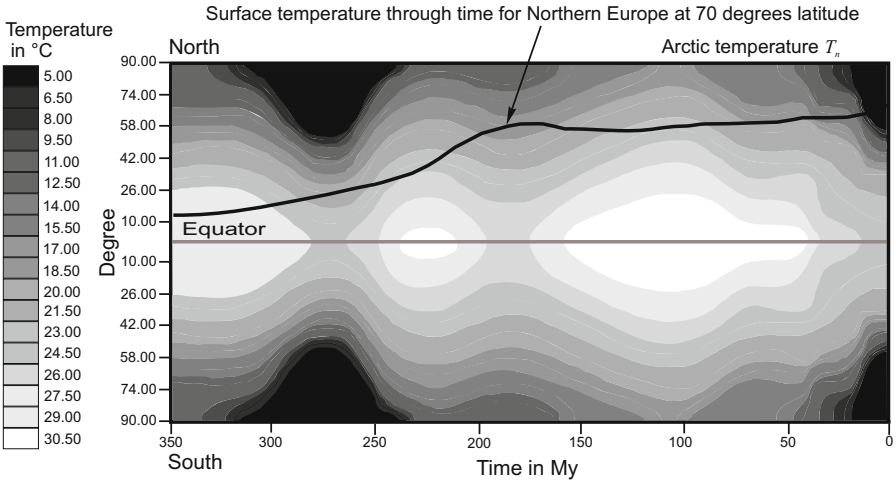

Fig. 3.23. Paleo–surface temperatures

$$T_{\mathrm{swi}}(0\,\mathrm{m}) = T_s, \quad T_{\mathrm{swi}}(200\,\mathrm{m}) = T_s - 3^{\circ}\mathrm{C}, \quad T_{\mathrm{swi}}(600\,\mathrm{m}) = T_n\ . \tag{3.33}$$

The average arctic temperature is about 4 °C at present, but it was much higher in the past (Fig. 3.23).

3.8 Crustal Models for Basal Heat Flow Prediction

Crustal models describe the mechanical and thermal processes of plate tectonics. In basin modeling, they are used to estimate the basal sediment heat flow as the lower boundary condition in the heat flow analysis (Fig. 3.1). Another

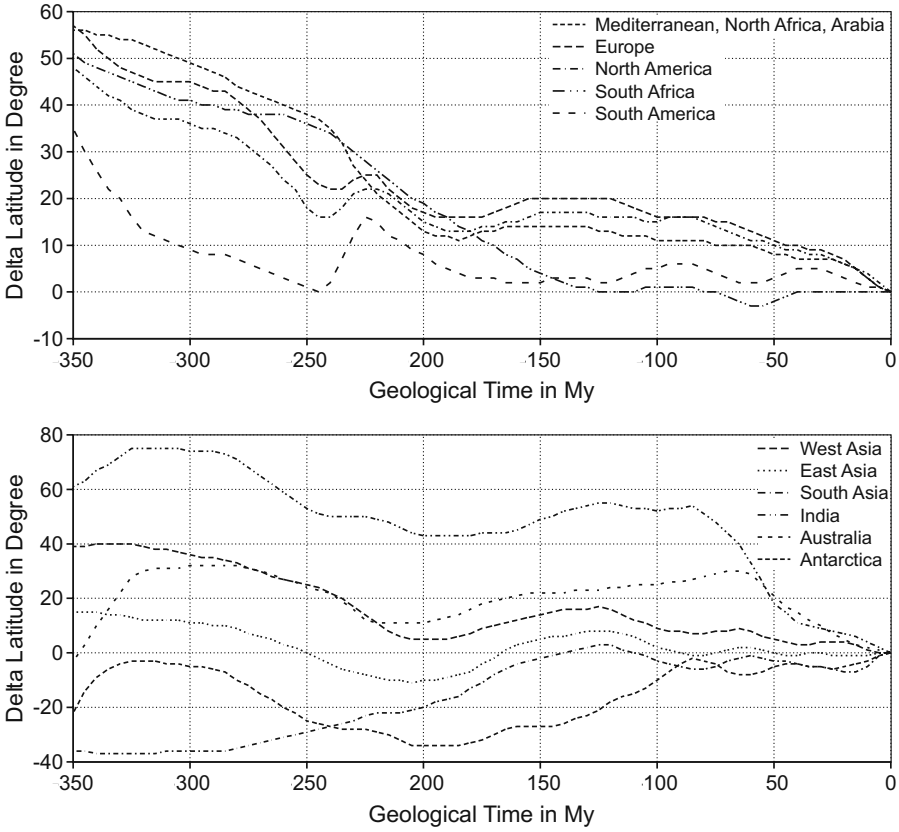

Fig. 3.24. Paleo latitude variations of some continental locations

interesting result of plate tectonic models is subsidence through time, which can be compared with sedimentation rates and paleo–water depths.

The asthenosphere, upper mantle, oceanic crust, lower and upper continental crust, and sediments are usually distinguished based on differences in their chemical compositions and mechanical properties as illustrated in Fig. 3.25. Mechanical behavior is the determining factor to distinguish between the solid lithosphere and the highly viscous (or pseudo–liquid) asthenosphere, which comprises the upper 250 km of the lower mantle. The lithosphere is further divided into the brittle upper crust and the ductile lower crust and upper mantle. Thus, faults are mainly formed in the upper crust during stretching of the lithosphere.

The classification between mantle and crust is based on chemical composition: mantle material mainly consists of mafic silicates, oceanic crust of mafic minerals and feldspar and continental crust of felsic silicates. There is evidence to assume that the entire mantle has a common convection system

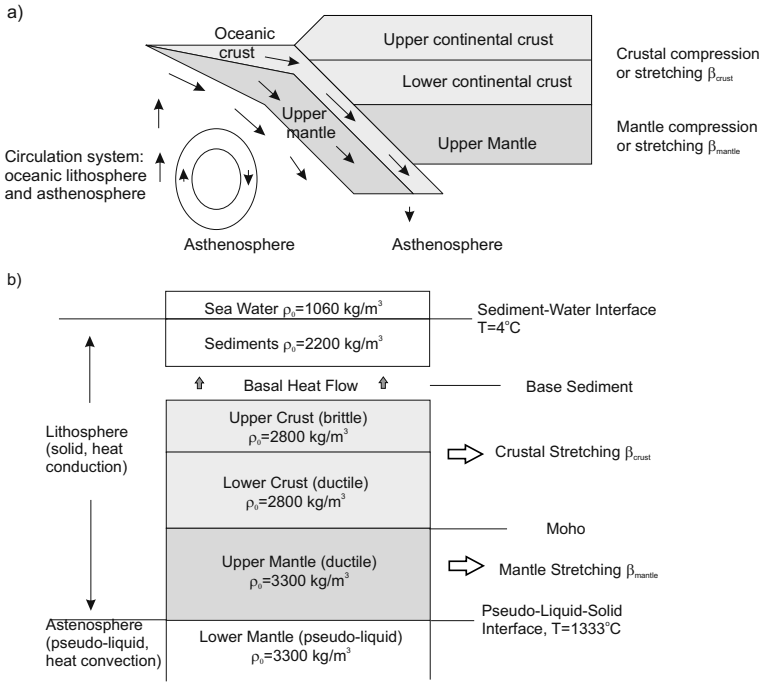

Fig. 3.25. Crust and mantle layer definitions. All rock densities are temperature dependent. The densities values ρ_0 are rock densities at surface conditions

with flow rates of about 10 to 20 cm/y. Oceanic crust, upper mantle and the asthenosphere have similar chemical compositions, since they build a closed circuit with constant formation of oceanic crust material at the mid–ocean ridges and destruction of it in the subduction zones. This circulation system also moves the continental crust pieces causing breakup, stretching, compression and overthrusting. The interface between the upper and lower mantle is the solid to pseudo–liquid boundary with a base lithosphere temperature of $T_a = 1100 - 1350\,°\mathrm{C}$. (Parsons and Sclater, 1977). The value of $T_a = 1333\,°\mathrm{C}$ is used in most publications (McKenzie, 1978), which corresponds to three quarters of the pyrolite melting temperature. The postulate of a fixed and well–known temperature at the base of the lithosphere, is an important assumption in crustal heat flow models.

Sediments are deposited in accommodation spaces as a result of lithospheric stretching and compression with usually different stretching velocities in the lithospheric layers and differences in deformation types. Crustal and mantle layers further differ in densities depending on their compositions and temperatures. Thus, a change in layer thicknesses, affects the weight of the total lithospheric column leading to subsidence with sedimentation on top or uplift with erosion. The depth of the top asthenosphere temperature isosur-

face and the thermal conductivities of the lithospheric layers primarily control the upward heat flow. In summary, a coupled model of lithospheric stretching, heat flow, and subsidence is necessary to obtain the base sediment heat flow through geologic time.

Plate tectonics yield different stretching, displacement, folding, and subduction processes especially on plate margins, which are related to different phases of basin development. Generalized models have been developed for a stable lithosphere in intra–plate locations, subduction zones at convergent margins and extensional rift–drift phases at divergent margins (Beardsmore and Cull, 2001).

Models of extensional rift basins are established since they can easily be quantified and because they can be applied to many petroleum provinces. The most thoroughly investigated and applied model is the model of uniform stretching, also known as the McKenzie model.

Uniform Stretching Model

This famous model was originally proposed by McKenzie (1978) and it is still frequently used with some minor improvements in basin analysis. It is based on two different periods: an initial stretching phase with constant thinning of the crust and upper mantle and a cooling phase with near or full restoration of the original thickness of the lithosphere. Here uniform stretching is not an uniform decrease of the layer thickness, instead it is a geological time–constant and linearly with depth increasing velocity field. Hence, the base of the lithosphere moves vertically at maximum speed, while the top of the lithosphere is fixed (Fig. 3.26). It also means that the speed of the base lithosphere decreases during uplift, which causes a slowdown in the thinning process.

The total thinning of the layers is described with a stretching factor β, which is the ratio of the initial to the final thickness. For the formulation of the heat transfer problem, it is more important to know the velocity vector of the moving layer element during stretching. The vertical component of the velocity v_z is linearly decreasing from bottom to top. The maximum velocity v_m is the velocity of the rock at the base of the lithosphere at the beginning of the stretching. The relationship between the stretching factor β, the stretching time t_s and the maximum velocity v_m is

$$t_s = \int_{h_0/\beta}^{h_0} \frac{h_0}{z\, v_m} dz = \frac{h_0 \log \beta}{v_m} \tag{3.34}$$

where h_0 is the initial thickness if the lithosphere.

The vertical component of the velocity at any depth $v_z(z)$ of the lithosphere during the entire stretching phase is

$$v_z(z) = \frac{z}{h_0}\, v_m \,. \tag{3.35}$$

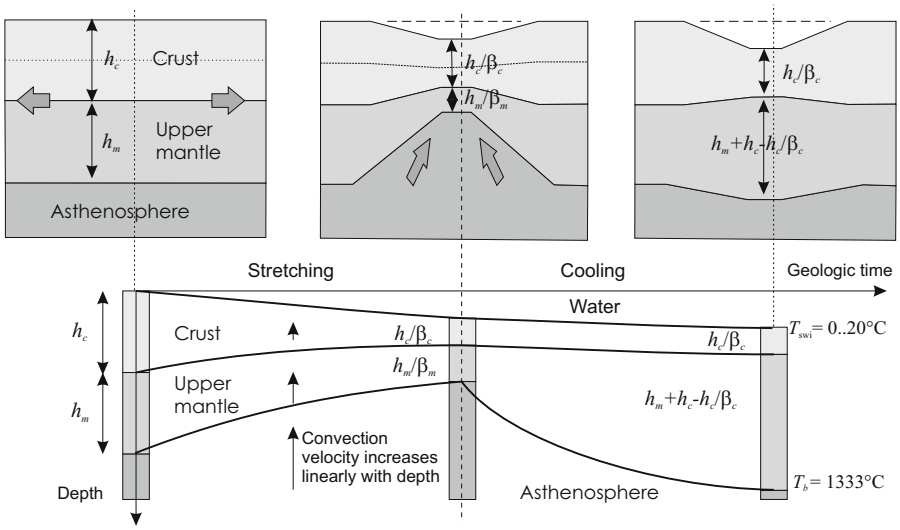

Fig. 3.26. McKenzie model with subsidence due to hydrostatic and isostatic compensation. The stretching velocity is constant in time and increases linearly with depth. This causes thinning of the crust and upper mantle during stretching. The original lithosphere thickness is restored during cooling

In this volume, it is usually dealt with two stretching factors for crust β_c and upper mantle β_m, and multi–1D heat conduction with radioactive heat production in the upper crust is considered.[2]

The model was originally worked out for symmetrical rifting, but it can also be applied to asymmetrical rifting and even compression, when each vertical lithospheric column experiences a phase of uniform thinning, which could be caused by stretching or sliding on detachment faults. Then, the stretching factors vary asymmetrically depending on their location as shown in Fig. 3.27 for the cases of pure shear, simple shear and simple shear–pure shear, respectively.

In the pure shear model, the vertical compressional deformation is equal to the horizontal extensional deformation as explained in Chap. 2. The simple shear model comprises only shear components and in the considered case, one large low angle detachment fault cutting through the entire lithosphere. Instead of extending along this detachment fault, the upper plate slips along the detachment surface. The simple shear–pure shear model considers simple shear in the crust and pure shear in the mantle. The corresponding stretching factor distributions along the section are mixtures of both end member models. The most realistic models are mixtures of the three stretching types, but some

[2] The original McKenzie model deals with one stretching factor only. Multiple stretching factors were introduced by Hellinger and Sclater (1983); Royden and Keen (1980)

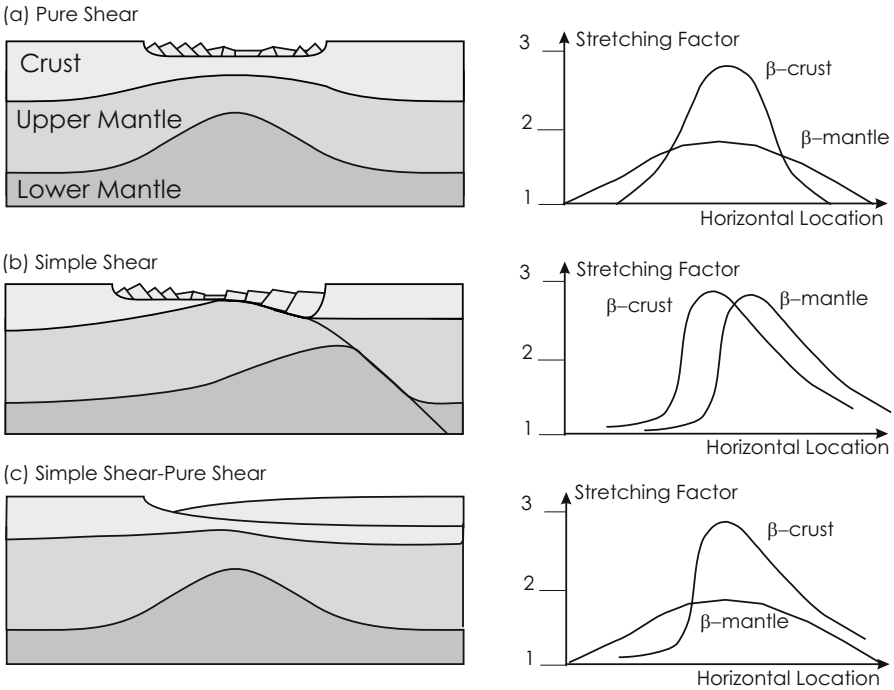

Fig. 3.27. Rift basins, according to Allen and Allen (2005): (a) pure shear, (b) simple shear, (c) simple shear–pure shear

can be approximated by the uniform stretching model when the stretching at each location can be described by only two single stretching parameters.

3.8.1 The Principle of Isostasy

The principle of hydrostatic isostasy states that the weight of all overburden material (lithosphere plus water depth) measured from a reference depth in the asthenosphere is constant. There is gravitational equilibrium between lithosphere and asthenosphere and the elevation depends on the underlying lithosphere column. An increase in lithospheric weight will therefore yield further subsidence so that the additional weight is compensated by the load of lighter water on top and less heavier asthenosphere at the base.

$$\rho_w g h_w + \sum_{i=0}^{n} \rho_{si} g h_{si} + \rho_{cu} g h_{cu} + \rho_{cl} g h_{cl} + \rho_m g h_m + \rho_a g h_a = \text{constant} \quad (3.36)$$

with the subscript indexes w, cu, cl, m, a for water, upper crust, lower crust, upper mantle, and asthenosphere, respectively and si for the ith sediment layer. This equation can be used to calculate water depths or mountain heights

from crustal layer thicknesses. The principle is illustrated for two very simple two layer (crust and mantle) models in Fig. 3.28: the Airy and the Platt model. The Airy model supposes a constant density for the entire crust. Thus, the mountain height or water depth is a simple function of the total crust thickness. Hence, the high mountains are above thick crust and large water depths suggest a thin crust below. The Platt model presumes a crust of varying density at the same depth level of the asthenosphere. Thus, the surface elevation is a function of the crustal density only: the higher the mountain the lighter the crust below. These examples illustrate the principle of a hydrostatic lithosphere: each vertical column of lithosphere is able to move independently of the adjacent column to balance itself via its own weight.

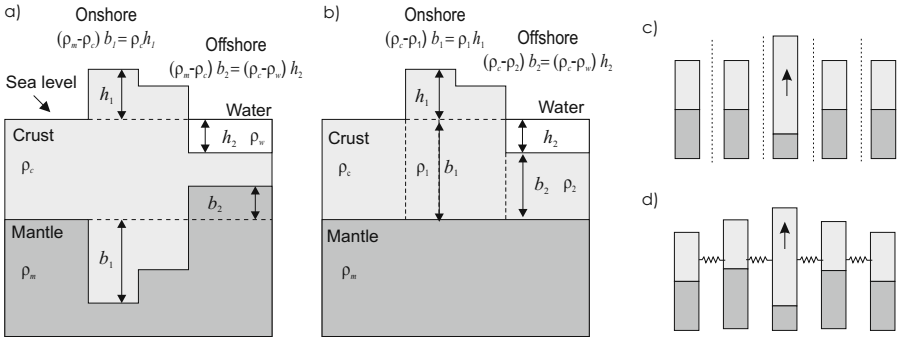

Fig. 3.28. Isostatic compensations: (a) Airy compensation. (b) Platt compensation. (c) Hydrostatic isostasy. (d) Flexural isostasy

In reality, there is an influence from the connected areas, which is described as flexural compensation, but which is not considered here. However, the weakness of the above models is the assumption of constant density with depth, since higher temperatures lower the density by thermal expansion according to

$$\rho(T) = \rho_0 \left[1 - \alpha(T - T_0)\right] \tag{3.37}$$

with the linear expansion factor $\alpha = 3.28 \times 10^{-5}/°\mathrm{C}$ (McKenzie, 1978) and a reference density ρ_0 for surface temperature $T_0 = 20\,°\mathrm{C}$. Another consequence of this equation is that cooling of the lithosphere causes subsidence and warming leads to uplift.

Uniform Stretching Model

The hydrostatic equation of isostasy applied to the uniform stretching model yields the following total mass per unit area for a column of water, crust, upper mantle and asthenosphere above a reference depth in the asthenosphere at any time (Fig. 3.26).

$$m = \rho_w\, h_w + \rho_{c0} \int_{h_w}^{d_c} [1 - \alpha_c T(x)] dx + \rho_{m0} \int_{d_c}^{d_m} [1 - \alpha_m T(x)] dx \\ + \rho_{m0} [1 - \alpha_m (T_a - T_{\text{swi}})]\, h_a \tag{3.38}$$

where α_c, α_m are the thermal expansions of the crust and mantle, and d_c, d_m are the depths of base crust and mantle, and h_w, h_a are the thicknesses of water and asthenosphere.

The tectonic water depths after instantaneous stretching h_{w_1} and after inifinite cooling h_{w_2} can be analytically calculated with the assumptions of no crustal radioactive heat production, a unique stretching factor β for crust and mantle, equal and constant thermal properties of the crust and mantle. and an linearly increase of the temperature with depth(Jarvis and McKenzie, 1980).

$$h_{w_1} = \frac{(h_m + h_c)\left[(\rho_{m0} - \rho_{c0}) \frac{h_c}{h_m + h_c} \left(1 - \alpha T_a \frac{h_c}{2h_m + 2h_c}\right) - \frac{\alpha T_a \rho_{m0}}{2}\right]\left(1 - \frac{1}{\beta}\right)}{\rho_{m0}(1 - \alpha T_a) - \rho_w}, \\ h_{w_2} = \frac{(\rho_{m0} - \rho_{c0}) h_c}{\rho_{m0}(1 - \alpha T_a) - \rho_w} \left[\left(1 - \frac{1}{\beta}\right) - \frac{\alpha T_a h_c}{2h_m + 2h_c} \left(1 - \frac{1}{\beta^2}\right)\right] . \tag{3.39}$$

The subsidence during stretching is related to an inflow of additional heavy asthenospheric material, while additional subsidence is caused by the cooling of the entire column. Again it should be noted, that the above premises, especially the assumption of instantaneous stretching as seen in equation (3.39) are drastic simplifications. More comprehensive equations should be used instead. Such subsidence curves through geological time are illustrated in Fig. 3.29 for various stretching factors. In Figs. 3.30 and 3.31 radioactive heat production in the crust is taken into account. The subsidence after stretching h_{w_1} can become negative (uplift), when crustal stretching is very small compared to mantle stretching, as shown in the example in Fig. 3.27.a at the margin of the pure shear model and in Fig. 3.32.b.

The subsidence is much larger, when the weight of the sediments is taken into account, in contrast to pure water filled basins. Total subsidence, which is the real subsidence with sediments is different from the tectonic subsidence, which is the theoretical subsidence for water fill only. The relation between tectonic subsidence h_w and total subsidence h_t is as follows:

$$h_t = \frac{\rho_a - \rho_w}{\rho_a} h_w + \frac{1}{\rho_a} \sum_{i=1}^{n} \rho_{si}\, h_{si} \tag{3.40}$$

where ρ_{si} and h_{si} are the density and thickness of the i-th sediment layer.

Sometimes, a basement is introduced between the upper crust and the sediments, which is the sediment package before stretching. It has to be determined whether the total and tectonic subsidence is then understood as the top or bottom basement.

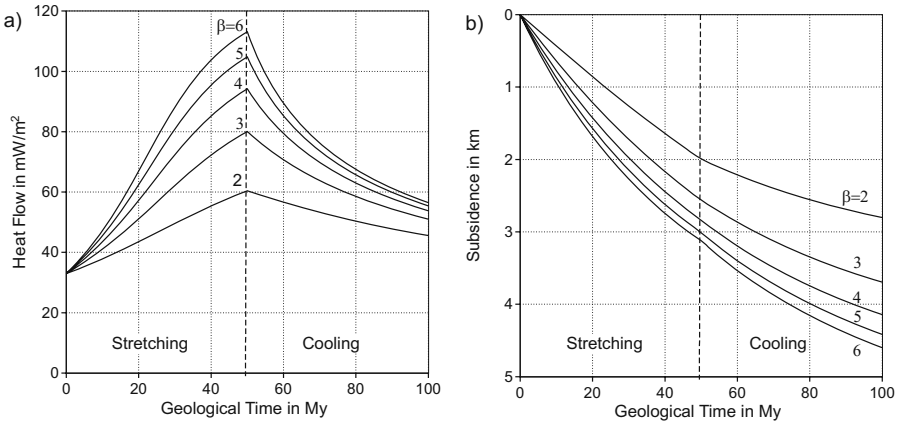

Fig. 3.29. McKenzie model: heat flow and tectonic subsidence for several stretching factors $\beta = \beta_c = \beta_m$ with $\kappa = 0.80410^{-6}\,\mathrm{m}^2/\mathrm{s}^{-1}$, $T_{\mathrm{swi}} = 0°\mathrm{C}$, $T_b = 1333°\mathrm{C}$, $h_c = 30\,\mathrm{km}$, $h_m = 95\,\mathrm{km}$ and $t_s = 50\,\mathrm{My}$

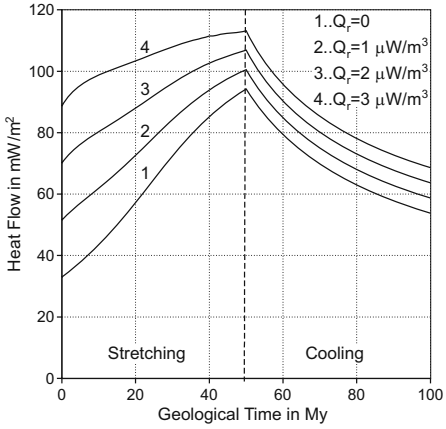

Fig. 3.30. Effect of constant radioactive heat production in the crust. The model parameters are the same as in Fig. 3.29 with the stretching factor $\beta = 4$

The principle of isostasy is universal, it is not restricted to pure shear processes only, e.g. basin subsidence and uplift can also be predicted in cases of underplating or other tectonic processes.

3.8.2 Heat Flow Models

The application of the 3D heat flow equation (3.29) to crustal models requires assumptions for thermal properties, boundary conditions and convection fields. The upper and lower boundary values are usually the sediment water interface and the top of the asthenosphere with the temperatures T_{swi} and T_a. Thermal conductivities and heat capacities of the upper crust depend on temperature as well as on rock composition. Radioactive heat production is

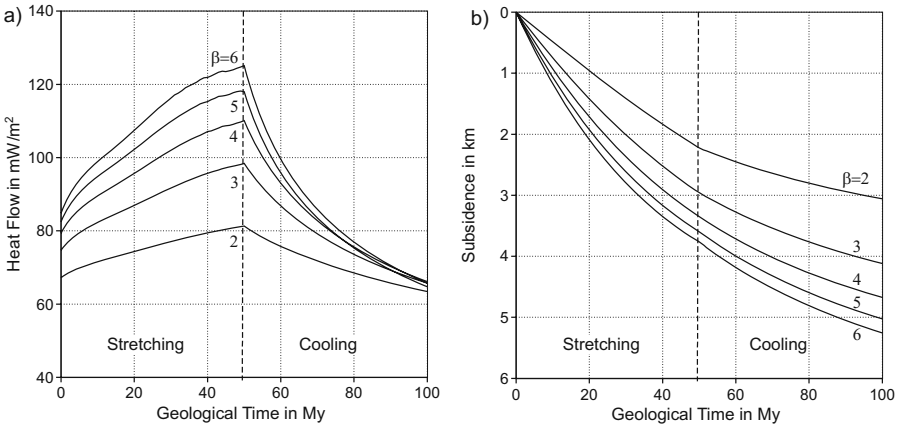

Fig. 3.31. Effect of exponentially decreasing radioactive heat production in the crust. The model parameters are the same as in Fig. 3.29 with $Q_{r0} = 2.5\,\mu\mathrm{W/m^3}$ and $z_h = 7\,\mathrm{km}$

known in the crust as an exponentially decreasing function with depth (Sclater et al., 1980; Allen and Allen, 2005). It can be expressed with the half–value depth z_h which describes the depth at which the concentration of radioactive elements is half the value of the maximum heat production Q_{r0}.

$$Q_r(z) = Q_{r0}\, 2^{-z/z_h} \; . \tag{3.41}$$

The convection term in (3.29) should be used for the moving lithosphere with velocity $\mathbf{v}$ and can be expressed with stretching factors for the crust and mantle (3.34). The problem is often approximated with a multi–1D solution, since horizontal crustal facies variations, together with extreme thermal conductivities, are assumed to be rather rare.

$$\lambda \frac{\partial^2 T}{\partial z^2} - \rho c \frac{\partial T}{\partial t} + \rho c v_z \frac{\partial T}{\partial z} + Q_r = 0 \; . \tag{3.42}$$

The vertical velocity field $v_z(z)$ can be derived from mechanical models. The stretching velocity increases linearly in the crust and mantle corresponding to the stretching factors, according to (3.34) and (3.35). It is

$$\lambda \frac{\partial^2 T}{\partial z^2} - \rho c \frac{\partial T}{\partial t} + \rho c \frac{\log \beta}{t_s}(h_0 - z) \frac{\partial T}{\partial z} + Q_r = 0 \tag{3.43}$$

where h_0 is the initial lithoshere thickness, and t_s is the stretching time. The thermal diffusivity $\kappa = \lambda/\rho/c$ is often given for the crust and mantle instead of the thermal conductivity λ. Note, that here $Q_r = 0$ in the mantle, $v_z = 0$ during cooling, and β is different for the crust and mantle.

The assumptions of the McKenzie model allow a solution of the heat flow equation with analytical methods. This is not possible when modifications of

the model are taken into account such as the introduction of radioactive heat production rates for the upper crust, different and variable thermal properties, and several stretching factors and stretching phases. Then, numerical integration methods such as finite difference methods can be applied.

The upward and downward movement of the highest asthenosphere surface during stretching and cooling yields the typical heat flow peaks for rift basins. Their height and width depends on stretching factors and stretching duration times (Fig. 3.29). Cooling has already an effect during the stretching phase and lowers the heat flow peak in the case of long stretching times. Thus, the maximum peak occurs at instantaneous stretching.

Without radioactivity, the heat flow declines to the initial value after infinite cooling, as the original lithosphere thickness is restored. Radioactive heat production of the crust increases the total heat flow towards the surface, but decreases the relative peak height compared to the initial value, since radioactive heat production decreases with thinning of the crustal layer (Fig. 3.30). This usually yields lower present day heat flow than the original values. Radioactive heat production also results in about 20% higher subsidence curves (Fig. 3.31) compared to models without radioactive heat production (Fig. 3.29). Thus radioactive heat production must not be neglected.

The upper mantle often has a higher stretching rate than the crust because it is more ductile. This also yields lower heat flow peaks and less subsidence compared to higher crustal thinning (Fig. 3.32). Heating the lithosphere with the highest rates at the beginning also has an uplift effect, which is usually balanced by the subsidence caused by crustal thinning. Fast and high mantle stretching and less crustal stretching allows the uplift effect to overcome subsidence, uplifting the basin when stretching starts (Fig. 3.32). Pure mantle stretching always results in uplift during stretching.

The above approach can easily be extended to several phases of uniform stretching with multiple pairs of stretching factors for rifting and cooling periods. Each stretching factor applies the actual thickness of the lithosphere when the new stretching period begins, instead of the initial thickness of the lithosphere (Fig. 3.33).

The linear velocity versus depth curve is independent of the total initial depth, it only depends on the stretching factor and time as expressed in equation (3.34), but the velocity $v_z(d_c)$ of the basal crust layer decreases exponentially in time, since it looses speed during uplift. Stretching factors are inconvenient for the description of any non–uniform stretching behavior. It is possible to work with velocity versus geological time functions instead, and the resulting heat flow equations can still be used in the above manner without any changes.

3.8.3 Workflow Crustal Preprocessing

Crustal models are useful to predict tectonic subsidence and paleo–heat flow when stretching and cooling behavior occurs. Present or paleo–subsidence

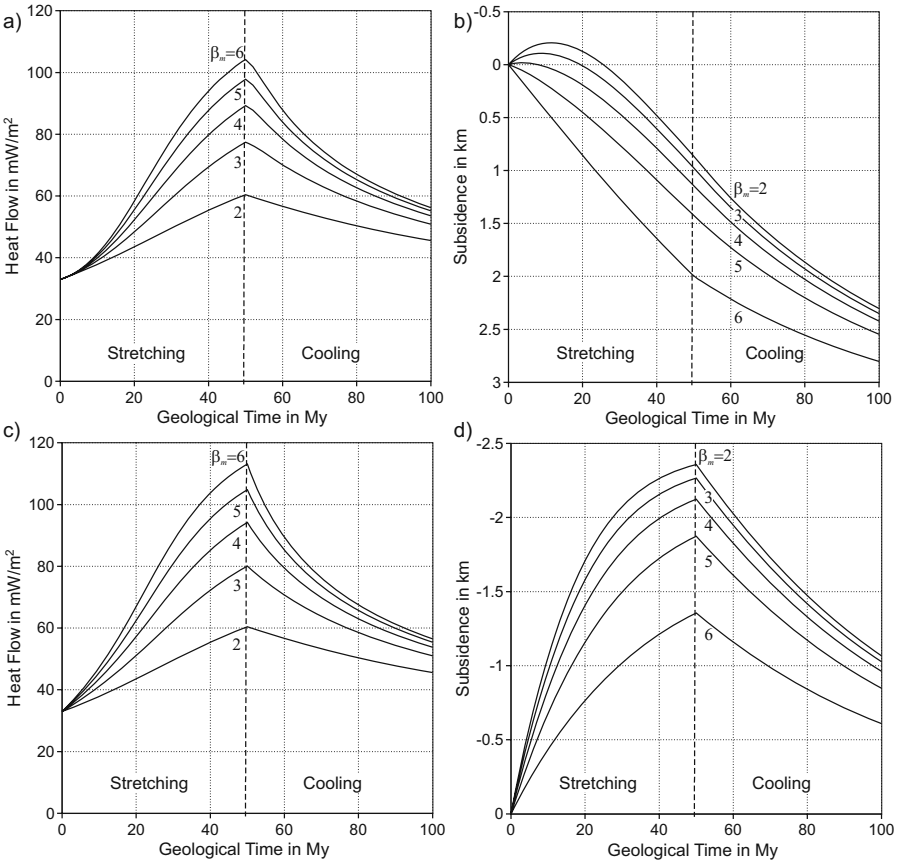

Fig. 3.32. Effect of different stretching factors for crust β_c and mantle β_m: (a),(b) small crustal stretching $\beta_c = 2$, (c),(d) no crustal stretching $\beta_c = 0$

from input geometry and stratigraphy can be used "inversely" to determine the stretching factors. The corresponding paleo–heat flow maps can then be calculated afterwards.

Fig. 3.34 illustrates the workflow for the calculation of paleo–heat flow maps from input geometry with calibrated stretching maps for crust and mantle using the uniform stretching model as described in the previous sections. It is also illustrated in Fig. 3.35.

The workflow starts with the extraction of the total paleo- and present day subsidence maps from the present day input model (Fig. 3.35.c). The corresponding back–stripping routine should also consider estimated paleo–water depth maps, decompaction and salt movement. Then, tectonic subsidence is calculated from total subsidence with the replacement of sediments by water (Eq. 3.40, Fig. 3.35.a). The main computing effort is then needed for inverting

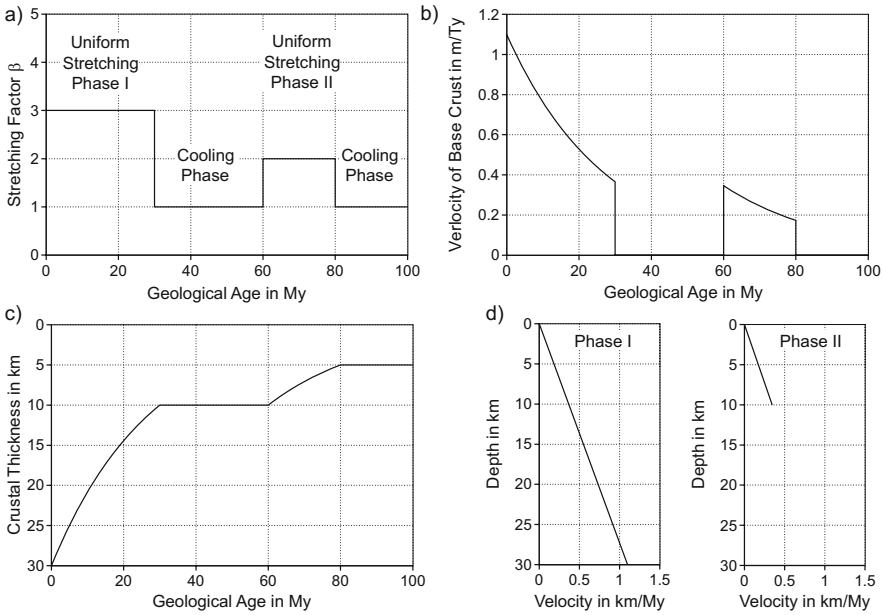

Fig. 3.33. Example with two uniform stretching periods, the initial crust thickness is 30 km: (a) Definition of the stretching and cooling periods. (b) The velocity of the base of the crust decreases exponentially during uplift. (c) The crustal thickness also decreases exponentially. (d) The time–constant velocity versus depth curve in the crust for the two stretching periods

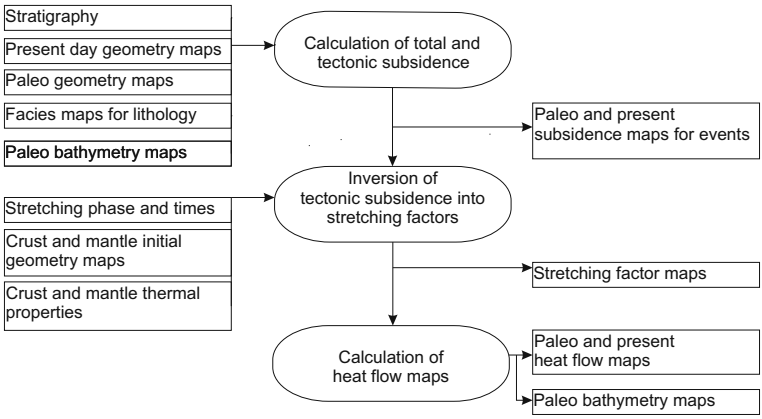

Fig. 3.34. Workflow for (crustal) heat flow preprocessor

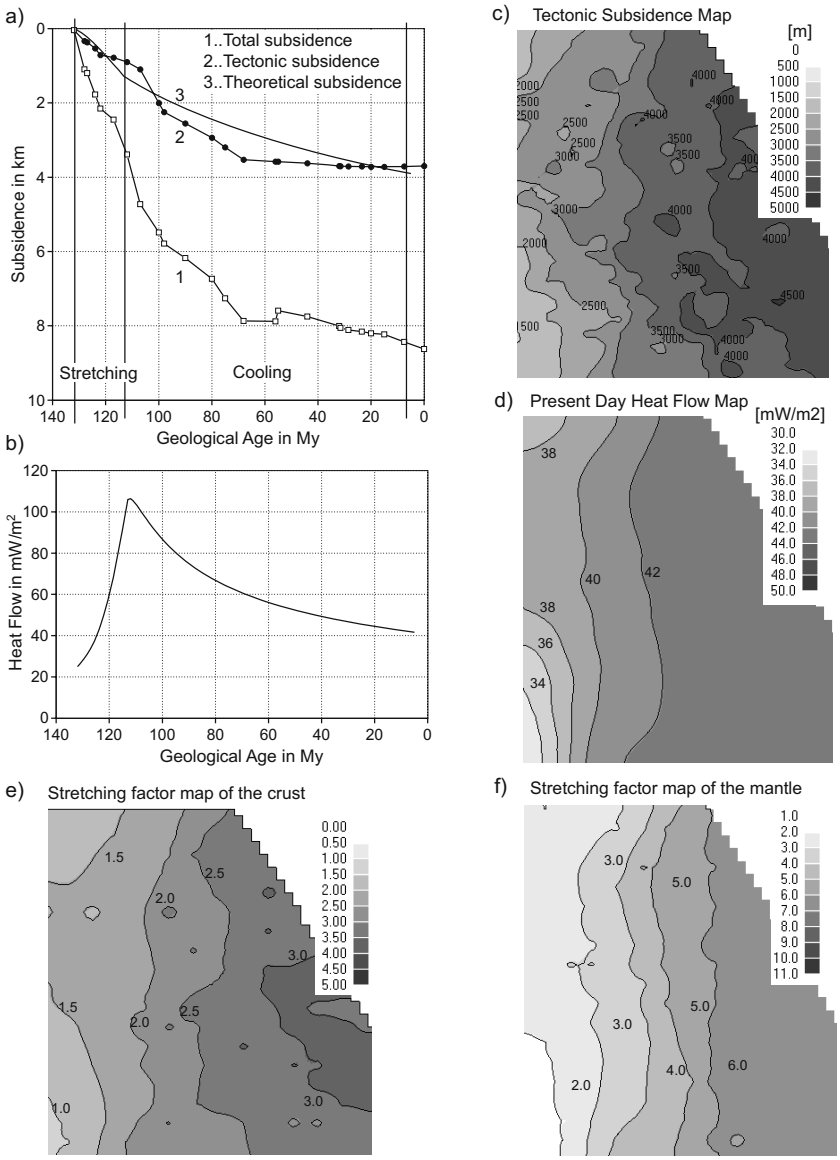

Fig. 3.35. Example from the Northern Campos basin for crustal heat flow analysis with a rift period of 132 − 113 My, $h_c = 35\,\mathrm{km}$, $h_m = 95\,\mathrm{km}$, $Q_{r0} = 2.5\mu\mathrm{W/m^3}$, $z_h = 7\,\mathrm{km}$: (a) Total and tectonic subsidence from input geometry and calculated theoretical subsidence after calibration at the location of the map midpoint. (b) Calculated heat flow at the basin midpoint with the calibrated stretching factors $\beta_c = 3.0$, $\beta_m = 4.7$. (c) Tectonic subsidence map from input geometry. (d) Calculated present day heat flow map. (e),(f) Maps with calibrated stretching factors for the crust and mantle

the tectonic subsidence maps into stretching factors, since it is an inversion of the heat and mechanical McKenzie type equations 3.43, 3.38. Usually, unique rifting and cooling times and initial crustal and mantle thicknesses are used for the entire map. The only unknowns in the inversion step are two stretching factors, which are calculated for each grid point in a multi–1D approach, so that the main output are two stretching maps for the crust and mantle (Fig. 3.35.e and f). The mantle map should be smoothed afterwards, if there is reason to assume high ductility.

The inversion can be performed for example with the response surface method, which is explained in Chap. 7. For each gridpoint 10 to 100 runs are necessary with the method of nesting intervals, so that there are about one million 1D forward simulation runs. The final stretching maps for crust and mantle can then be used to calculate the paleo and present heat flow maps through time and to recalculate the paleo water depth maps from simulated subsidence values.

This workflow can be extended to more than one rifting event or to define and calibrate other unknowns of the model, such as the initial thickness of the crust. Three stretching maps for the upper and lower crust and the mantle can also be used instead of the presented two layer model, or the two stretching maps can be assigned to upper crust and lower crust/upper mantle, respectively. Gravitational data can also be used for additional calibration parameters, e.g. when the crust geometry directly controls gravity.

Another less accurate and much simpler procedure is use of McKenzie's equilibrium subsidence (3.39) to directly calculate the stretching factor maps from the total present day subsidence map only, and to predict the paleo–heat flow maps and the new water depth maps afterwards.

It is obvious that the McKenzie type models yield only rough estimates of the basal heat flow maps through time and the heat flow maps need to be fine tuned with vitrinite reflectance data and bottom hole temperatures afterwards. A decoupling of the procedures in the two steps of crustal preprocessing and calibration against the thermal markers, allows a better overview and handling of the individual parts and leads to a better understanding of the respective processes.

3.9 Heat Flow Calibration

Heat flow models can be calibrated with measured temperatures from wells and thermal maturity parameters, such as vitrinite reflectance, biomarkers and fission–track annealing data. Thermal maturity parameters are time and temperature dependent. They indicate how long the rock elements remain at certain temperature levels. Thus, single data points of specific thermal markers are often only useful to calibrate a small temperature interval. They cannot be used to specify a total age for the temperature interval. Exceptions are fluid inclusion temperatures, which are often related to paleo–ages.

The most commonly used parameter is vitrinite reflectance, since it is widely available in most sediment types, covers typical oil and gas maturity ranges and is easy and cheap to measure. The importance and main temperature windows of many other thermal markers are compared and explained in more detail in Chap. 4. The most uncertain input parameters are thermal conductivity and paleo- and present basal heat flow values.

There are several workflows and techniques developed to change thermal conductivity and heat flow parameters, when thermal maturity data or measured temperatures, differ from a master run. Recently, more emphasis has been put on the calibration of basal heat flow values as thermal conductivities are much better known. The assumption of a rift–type heat flow peak or any other trend can be obtained as a first estimation from crustal models or other knowledge about geological history. Such trends are typically defined for individual locations and usually calibrated against well data such as bottom hole temperatures or vitrinite reflectance values. The heat flow trends can then be simply shifted entirely or stepwise or other corrections like first order shifting or heat flow peak calibration can be performed until the match with the calibration data is satisfying (Fig. 3.36).

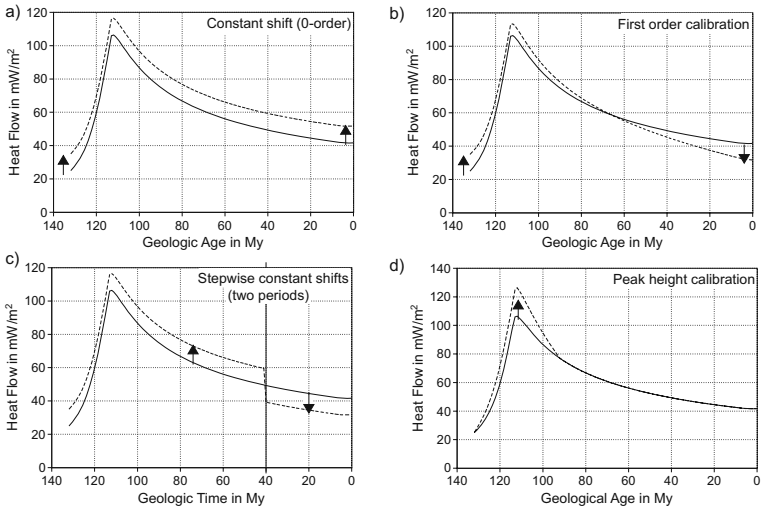

Fig. 3.36. Methods of heat flow trend calibration: (a) Constant shift. (b) First order calibration. (c) Stepwise constant shifts. (d) Special peak height change

Automatic calibration tools can be used, when numerous thermal calibration parameters are available. They allow the definition of time intervals with independent shift corrections, peak corrections or the assumption of additional uncertainties for SWI temperatures or thermal properties. Numerical models used for the automatic calibration or inversion are Monte Carlo sim-

ulations, response surface modeling or fast approximated forward simulation techniques, all of which are described in the Chap. 7. One typical workflow of an automatic 3D calibration processor is described below.

The final values of an automatic calibration must make physical and geological sense, rather than simply providing an acceptable mathematical fit between measured and calculated values. This is achieved with fixed parameter ranges or the Bayesian approach (Chap. 7).

3.9.1 Example Workflow for 3D Heat Calibration

The workflow under discussion is illustrated in Fig. 3.37. A fit to calibration data such as temperature and vitrinite reflectance values should obviously be achieved while conserving the shape of the heat flow trend through time. Here, only a constant shift of the heat flow trends is considered. The procedure can be applied to regions of limited size, typically to small areas of interest around a well or a group of wells (Fig. 3.38). The extension of these areas should be large enough to incorporate lateral heat flow effects as they appear e.g. in the vicinity of salt domes. The temperature evolution inside each area can be fitted with its own heat flow shift.

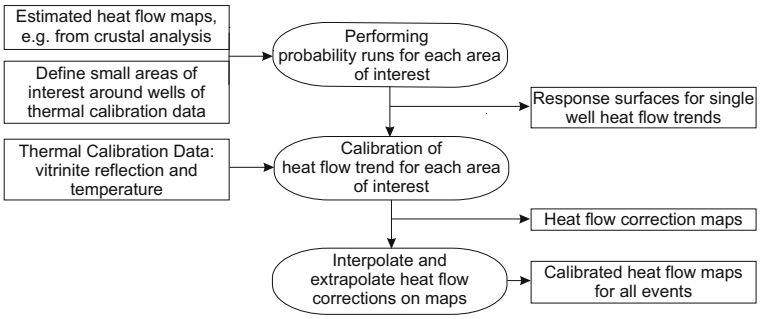

Fig. 3.37. Workflow for heat flow preprocessor

A calibration performed in any area of interest is independent of calibrations in other areas. Therefore, it can, for example, be performed in a separate "mini–model".[3] In practice many wells with calibration data are available and it is advantageous to run all the areas together in one big 3D simulation. The areas around the wells are restricted to a small size. As smaller these sizes as the faster the simulation. This is important in practice, because multiple runs with varying heat flow must be performed.[4] The calibration in each area

[3] If lateral heat flow effects are neglected such a "mini–model" becomes a pure 1D–model.

[4] When sufficient computer resources are available, it is also possible to run the full 3D model without any areal cut–outs. This would reproduce all 3D thermal

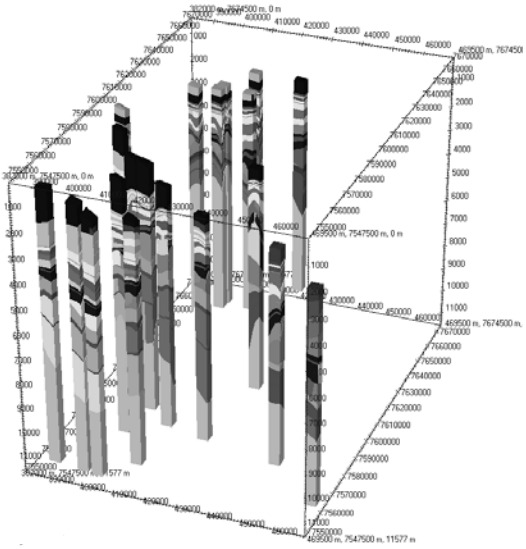

Fig. 3.38. Example of a heat flow calibration in areas around wells with temperature and vitrinite reflectance data. The size of each area is equivalent to the thickness of the corresponding column. These column thicknesses are defined as rather thin here because lateral heat flow effects are small

is performed independently of each other afterwards. Advanced interpolation and extrapolation between different simulation results with, for example, response surfaces as described in section Sec. 7.5.1, yield fast and accurate results (Figs. 3.39, 3.40).

Finally, calibrated heat flow maps can be constructed by spatial interpolation between the areas with calibrated heat flow shifts. If necessary, an additional smoothing of the interpolated heat flow shift can be performed. The results can be tested in a final simulation run.

Crustal heat flow analysis and heat flow calibration can be performed successively (Fig. 3.41). It is thus possible to construct calibrated and geological meaningful heat flow maps from a basin model and additional geological information about stretching phases, crustal structure, bottom hole temperatures and vitrinite reflectance data.

---

effects. However, calibrated heat flow shifts below each calibration well, must be assigned to limited areas for further construction of new structural heat flow maps by interpolation. Additionally, these areas should not be too small. Otherwise in the full 3D model, heat might leave these areas laterally due to lateral temperature gradients. This may yield too low temperatures at the well locations and the calibration might fail.

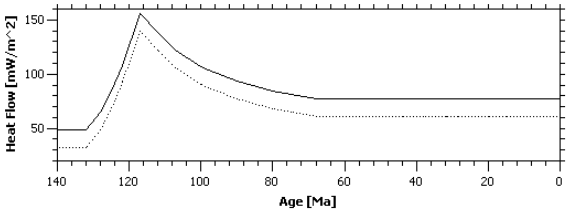

Fig. 3.39. Shifted heat flow trend after calibration (solid line) and before calibration (dotted line)

Fig. 3.40. Temperature and vitrinite reflectance in the same well calibrated against data values with error bars. Dotted lines represent results from a crustal model only. The corresponding heat flow shift is shown in Fig. 3.39. Note that a fit against temperature data alone would yield a slightly lower temperature and vitrinite reflectance profile. However, due to small error bars vitrinite reflectance values are treated here with higher importance than temperature values

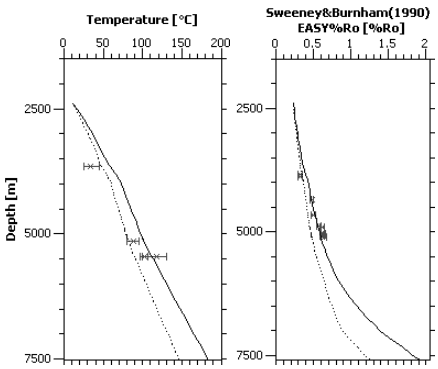

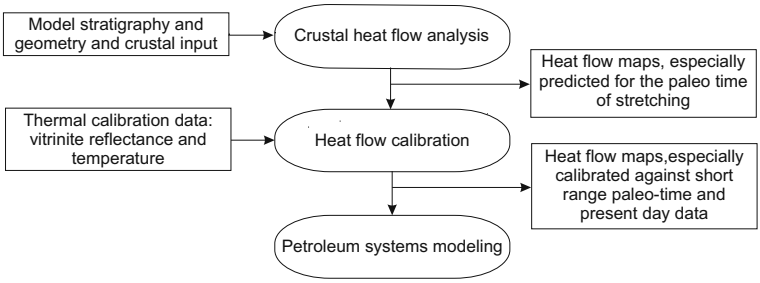

Fig. 3.41. General workflow, which links crustal modeling, heat flow calibration and petroleum systems modeling

Summary: Heat flow analysis is based on a detailed balance of thermal energy that is transported via heat flow through sedimentary basins. Heat flow occurs primarily in form of conduction and convection. The driving forces for conduction are temperature differences. Convection is classified by moving fluid or solid phases that carry their inner thermal energy along. Previously to a detailed energy balance it is necessary to specify heat in– and outflow or alternatively the temperature at the boundary of the sedimentary basin.

The main direction of heat flow in sedimentary basins is vertically upwards. It is thus possible to demonstrate basic effects with crude one dimensional models. Steady state heat flow constitutes the most simple heat flow pattern. Explicit formulas can be calculated. Radioactive heat production can easily be incorporated. The complexity of the system rises with consideration of transient effects which occur during deposition, erosion, and when thermal boundary conditions change. However, some idealized special cases can be solved analytically.

The main thermal properties of the rocks are thermal conductivities, readiogenic heat production, and heat capacities. Detailed specifications of these properties for various lithologies and fluids over wide temperature ranges are well known.

The general formulation of two and three dimensional heat flow problems incorporates heat convection and magmatic intrusions. The quantification of heat flow and temperature boundary conditions is often a major task. SWI temperatures can be derived from paleo climate models. Effects of permafrost require the specification of paleo surface temperatures.

Basal heat flow can be calculated from tectonic stretching and thinning of the crust which causes the evolution of the basin. Models for rift basins are mainly worked out as extensions to the famous McKenzie type crustal models. Basic principles are isostasy and crustal heat flow balance. Finally, the amount of stretching can be calibrated against the known subsidence of the sedimentary package. Comprehensive heat flow trends can be constructed.

These trends can locally be adapted to known temperature histories from well logs and samples, e.g. bottom hole temperatures and vitrinite reflectance measurements. Sophisticated workflows are worked out for fast and efficient calibration procedures.